



Craton destruction links to the interaction between subduction and mid-lithospheric discontinuity: Implications for the eastern North China Craton

Ya-Nan Shi ^{a,b}, Fenglin Niu ^{a,b}, Zhong-Hai Li ^{c,*}, Pengpeng Huangfu ^c

^a State Key Laboratory of Petroleum Resources and Prospecting, Unconventional Petroleum Research Institute, China University of Petroleum at Beijing, Beijing, China

^b Department of Earth, Environmental and Planetary Sciences, Rice University, Houston, TX, USA

^c Key Laboratory of Computational Geodynamics, College of Earth and Planetary Sciences, University of Chinese Academy of Sciences, Beijing, China

ARTICLE INFO

Article history:

Received 17 July 2019

Received in revised form 16 January 2020

Accepted 16 January 2020

Available online 28 February 2020

Handling Editor: T. Gerya

Keywords:

Craton destruction

Mid-lithosphere discontinuity

Oceanic plate subduction

North China Craton

Numerical modeling

ABSTRACT

The continental craton is generally considered to be stable, due to its low-density and high viscosity; however, the thinning and destruction of cratonic lithosphere have been observed at various parts of the globe, for example, the eastern North China Craton (NCC). Although a large number of geological and geophysical data have been collected to study the NCC, the mechanisms and dynamic processes are still widely debated. In this study, using 2-D high-resolution thermo-mechanical models, we systematically explore the key constraints on the destruction of cratonic lithosphere. The model results indicate that the craton destruction processes can be strongly influenced by the presence of the so-called mid-lithosphere discontinuity (MLD), and its interaction with subduction. The properties of the MLD layer and the density contrast between the lithospheric mantle and asthenosphere play significant roles in the destruction processes. Specifically, the presence of a deep and low-viscosity MLD layer within the cratonic lithosphere tends to enhance instability of the craton, making it easier for lithosphere destruction. In addition, a relatively thick oceanic crust, high convergence rate, and large initial subduction angles favor the craton destruction. Finally, we compare the model results with the observations of NCC, which indicate that the interaction between the Paleo-Pacific subduction and the MLD layer in the cratonic lithosphere has played an important role in the observed large-scale lithospheric removal of the eastern North China Craton.

© 2020 International Association for Gondwana Research. Published by Elsevier B.V. All rights reserved.

1. Introduction

Craton is a stable continental lithosphere with a thickness of around 200–300 km that exists for billions of years on the Earth's surface (Jordan, 1988; Griffin et al., 1998; Sleep, 2003; Menzies et al., 2007). Their low density and high viscosity retain them above the weak asthenosphere without destruction by long-term geological processes (Schubert et al., 2001; Lee et al., 2011; Wu et al., 2014). However, many studies revealed that several cratons have experienced significant lithospheric thinning, partial or complete removal after the initial building and stabilization stage (e.g., Wu et al., 2014; Liu and Li, 2018). For example, the lithosphere beneath the eastern part of the North China Craton (NCC) is ~100 km thinner than that of the western part (Fig. 1). The lithospheric thinning is speculated to have occurred in the Mesozoic, together with large-scale magmatic activities (Lu et al., 1991; Menzies et al., 1998; Carlson et al., 2005; Zhu et al., 2012; Wu et al., 2019). The mantle lithospheres beneath the Indian, Siberian and

South American cratons are estimated to be thinned by ~120 km (Rao et al., 2001, 2013; Dessai et al., 2004; Kumar et al., 2007; Karmalkar et al., 2009; Wu et al., 2014), ~50 km (Griffin et al., 1999b; Howarth et al., 2014), and ~75 km (Read et al., 2004), respectively.

Based on the systematic geological and geophysical observations, many mechanisms have been proposed to explain the thinning and destruction of cratonic lithosphere (Liu and Li, 2018; and references therein). For the NCC, it is generally proposed that the destruction in Mesozoic is controlled by the Paleo-Pacific subduction (Zhu et al., 2012; and references therein), in which the subduction-induced partial melting may weaken the overriding lithosphere and gradually lead to the alteration of mantle lithosphere. Windley et al. (2010) suggested that the destruction of NCC was closely related to the hydration process during the Paleo-Pacific subduction, which significantly decreased the viscosity of the cratonic keel. Wang et al. (2016) found two series of magmatism during the destruction of NCC, which are, respectively, related to (i) the perturbation of hydrous mantle transition zone by the subducted Izanagi plate in the period of ~135–115 Ma, and (ii) the asthenospheric partial melting and lithospheric extension by the rollback of Pacific plate at ~80 Ma in Cenozoic. In addition, the viscosity of the big

* Corresponding author.

E-mail address: li.zhonghai@ucas.ac.cn (Z.-H. Li).

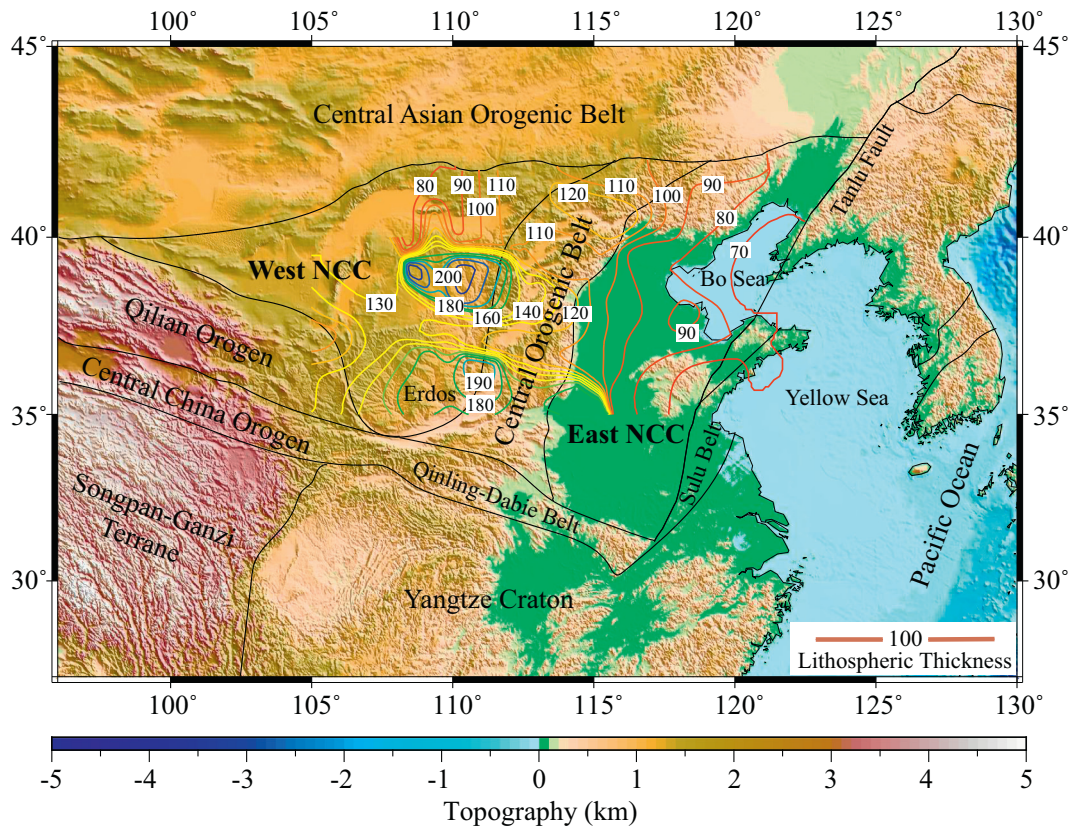


Fig. 1. Tectonic map of the North China Craton (NCC), which is modified from Zhu et al. (2012), and Liu and Li (2018). Different colors represent the topography. Values of lithospheric thicknesses are from the open-sourced dataset (<http://www.craton.cn/data>) (Chen, 2009, 2010; Chen et al., 2008, 2009, 2014; Zheng et al., 2017).

mantle wedge could be decreased due to the dehydration of the subducting plate, which thereby contributes to the vigorous mantle convection and an increase in heat flow at the base of the lithosphere (He, 2014).

Recent seismic studies, on the other hand, found a single or multiple velocity discontinuities in the middle of the cratonic lithosphere (e.g., Chen, 2017 and references therein), which is known as the mid-lithosphere discontinuity (MLD) or discontinuities (MLDs). The MLDs are mostly observed at ~80–100 km depth with a thickness of ~20–40 km (Abt et al., 2010; Yuan and Romanowicz, 2010; Chen et al., 2014; Hopper et al., 2014; Selway et al., 2015; Nita et al., 2016; Aulbach et al., 2017; Kennett and Sippl, 2018; Sun et al., 2018). The thickness, depth, potential origins and rheological properties of the MLD are still not well constrained (Karato et al., 2015; Selway et al., 2015; Aulbach et al., 2017; Wang and Kusky, 2019). Various mechanisms have been proposed for the nature of the MLDs (Thybo and Perchuc, 1997; Yuan and Romanowicz, 2010; Xu, 2001; Wölbner et al., 2012; Karato et al., 2015; Wang and Kusky, 2019), such as (1) metasomatism, i.e., through the enrichment of pyroxene, phlogopite, amphibole, carbonatite, infiltrated frozen melts (Thybo and Perchuc, 1997; Xu, 2001; Abt et al., 2010; Wölbner et al., 2012; Sodoudi et al., 2013; Rader et al., 2015; Selway et al., 2015; Wang Z et al., 2016; Aulbach et al., 2017); (2) elastically-accommodated grain boundary sliding (Karato et al., 2015); and (3) change in azimuthal anisotropy (minerals with distinct orientation) (Tommasi et al., 2009; Yuan and Romanowicz, 2010; Hansen et al., 2012). Regardless of nature, the MLD layer is generally considered to be rheologically weaker than the upper and lower parts of the lithosphere (Wang and Kusky, 2019). Further numerical studies have demonstrated that a weak MLD layer can significantly promote deformation and destruction of cratonic lithosphere under different tectonic settings (Wang and Kusky, 2019). Under extension and rifting setting, the existence of a weak MLD could accelerate the deformation of the overlying mantle and the crust (Liao et al., 2013; Liao

and Gerya, 2014). A rapid delamination of the lower lithospheric mantle could be also caused by the contact of MLD with a hot asthenosphere (Wang et al., 2018; Liu et al., 2018a, 2018b).

Based on the above discussion, both subduction and MLD may play certain roles in the craton destruction; however, their effects are generally isolated in the previous modeling. Here we present a series of numerical experiments based on a two-dimensional (2-D) high-resolution thermo-mechanical model, in which we have tested the sensitivities of various MLD properties and subduction conditions on the craton thinning and destruction.

2. Numerical methodology

2.1. Governing equations

For the numerical modeling we used a finite-difference numerical code (I2VIS) with a marker-in-cell technique (Gerya and Yuen, 2003a). The momentum, continuity and heat conservation equations for a 2D creeping flow including thermal and chemical buoyant forces were solved within this code.

(1) 2D stokes equations:

$$\begin{aligned} \frac{\partial \sigma'_{xx}}{\partial x} + \frac{\partial \sigma'_{xz}}{\partial z} &= \frac{\partial P}{\partial x} \\ \frac{\partial \sigma'_{zx}}{\partial x} + \frac{\partial \sigma'_{zz}}{\partial z} &= \frac{\partial P}{\partial z} - g\rho(C, M, P, T) \end{aligned} \quad (1)$$

where x and z are respectively horizontal and vertical coordinates; g is gravitational acceleration; σ'_{ij} are components of deviatoric stress tensor; and the density ρ depends on composition (C), melt fraction (M), temperature (T) and pressure (P).

- (2) Conservation of mass is approximated by the incompressible continuity equation:

$$\frac{\partial v_x}{\partial x} + \frac{\partial v_z}{\partial z} = 0 \quad (2)$$

where v_x and v_z are velocity components.

- (3) Heat conservation equation:

$$\begin{aligned} \rho C_p \left(\frac{DT}{Dt} \right) &= -\frac{\partial q_x}{\partial x} - \frac{\partial q_z}{\partial z} + H_r + H_a + H_s q_x = -k(T, P, C) \frac{\partial T}{\partial x} q_z \\ &= -k(T, P, C) \frac{\partial T}{\partial z} H_a = T \alpha \frac{dP}{dt} H_s \\ &= \sigma'_{xx} \varepsilon_{xx} + \sigma'_{zz} \varepsilon_{zz} + 2\sigma'_{xz} \varepsilon_{xz} \end{aligned} \quad (3)$$

where C_p is the effective isobaric heat capacity; DT/Dt is the substantive time derivative of temperature; q_x and q_z are heat flux components; H_r , H_a , and H_s denote radioactive heat production, the energetic effect of isothermal (de)compression (i.e., adiabatic heating/cooling), and shear heating, respectively; $k(T, P, C)$ is the thermal conductivity as a function of temperature, pressure and composition (Hofmeister, 1999); α is the thermal expansion coefficient; ε_{ij} is the strain rate tensor.

2.2. Rheological model

The relationship between the deviatoric stress (σ'_{ij}) and the strain rate (ε_{ij}) tensors are described by realistic visco-plastic constitutive laws. In case of incompressible viscous deformation, the viscous law of friction is:

$$\begin{aligned} \sigma'_{xx} &= 2\eta_{eff} \varepsilon_{xx} \varepsilon_{xx} = \frac{\partial v_x}{\partial x} \sigma'_{xz} = 2\eta_{eff} \varepsilon_{xz} \varepsilon_{xz} \\ &= \frac{1}{2} \left(\frac{\partial v_x}{\partial z} + \frac{\partial v_z}{\partial x} \right) \sigma'_{zz} = 2\eta_{eff} \varepsilon_{zz} \varepsilon_{zz} = \frac{\partial v_z}{\partial z} \end{aligned} \quad (4)$$

where η_{eff} is the effective viscosity that depends on the pressure, temperature, composition, strain rate and degree of melting.

For rocks containing a small fraction of melts ($M < 0.1$, M is the volumetric melt fraction), the effective viscosity for viscous creep ($\eta_{ductile}$) as a function of pressure, temperature, composition and strain rate invariant is defined by:

$$\eta_{ductile} = (\varepsilon_{II})^{\frac{1-n}{n}} (A_D)^{\frac{1}{n}} \exp\left(\frac{E+PV}{nRT}\right) \quad (5)$$

where $\varepsilon_{II} = (0.5\varepsilon_{ij}\varepsilon_{ij})^{1/2}$ is the second invariant of the strain rate tensor; and n , A_D , E , and V are experimentally determined flow law parameters, which stand for stress exponent, material constant, activation energy, and activation volume, respectively. In addition, we define η_0 as the pre-exponential viscous factor, which is calculated by $\eta_0 = (1/A_D) \times 10^{6n}$.

The viscous rheology is combined with a brittle/plastic rheology to yield an effective visco-plastic rheology. For this purpose, the extended Drucker-Prager yield criterion (Ranalli, 1995) is implemented as follows:

$$\sigma_{yield} = C_0 + P \sin(\varphi_{eff}) \quad \sin(\varphi_{eff}) = \sin(\varphi)(1-\lambda) \quad \eta_{plastic} = \frac{\sigma_{yield}}{2\varepsilon_{II}} \quad (6)$$

where σ_{yield} is the yield stress; C_0 is the cohesion and φ is the internal frictional angle; P is the dynamic pressure; φ_{eff} can be illustrated as the effective internal angle (φ) and pore fluid coefficient (λ) that controls the brittle strength of fluid-containing porous or fractured media (Brace and Kohlstedt, 1980); ε_{II} is the second invariant of the strain

rate tensor. In this paper, the aqueous fluid activity, i.e., the (de)hydration process, is not modeled directly. Thus, the plastic rheology is implemented by variable values of $\sin(\varphi_{eff})$ for different rock types, based on previous systematic investigations (e.g., Li et al., 2016).

With the $\eta_{ductile}$ and $\eta_{plastic}$, the visco-plastic rheology is assigned to the model by means of a Christmas tree-like criterion, where the rheological behavior depends on the minimum viscosity attained between the viscous and brittle/plastic fields (Ranalli, 1995).

$$\eta_{creep} = \min(\eta_{viscous}, \eta_{plastic}) \quad (7)$$

2.3. Partial melting

The numerical code accounts for partial melting of the various crustal lithologies using experimentally obtained P - T dependent wet solidus and dry liquidus curves (Gerya and Yuen, 2003b). Volumetric melt fraction M is assumed to increase linearly with temperature according to the following relations (Burg and Gerya, 2005):

$$M = \begin{cases} 0 & T \leq T_{solidus} \\ \frac{T - T_{solidus}}{T_{liquidus} - T_{solidus}} & T_{solidus} \leq T \leq T_{liquidus} \\ 1 & T \geq T_{liquidus} \end{cases} \quad (8)$$

where $T_{solidus}$ and $T_{liquidus}$ are the wet solidus and dry liquidus temperature of the given lithology, respectively. Due to the lack of aqueous fluid activity in this study, the partial melting of dry mantle rock is rather difficult, which is thus neglected. The direct simulation of subduction-induced deep hydration and partial melting can be found in Li et al. (2019).

Consequently, the effective density (ρ_{eff}) of partially molten rocks varies with the amount of melt fraction and P - T conditions according to the relations:

$$\rho_{eff} = \rho_{solid} - M(\rho_{solid} - \rho_{molten}) \quad (9)$$

where ρ_{solid} and ρ_{molten} are the densities of the solid and molten rock, respectively, which change with pressure and temperature according to the following relation:

$$\rho_{P,T} = \rho_0 [1 - \alpha(T - T_0)] [1 + \beta(P - P_0)] \quad (10)$$

where ρ_0 is the standard density at $P_0 = 0.1$ MPa and $T_0 = 298$ K; α is thermal expansion coefficient; β is compressibility coefficient.

The effects of latent heat (Stüwe, 1995) are accounted by an increased effective heat capacity (C_{peff}) and thermal expansion (α_{eff}) of the partially molten rocks ($0 < M < 1$), expressed as

$$\begin{aligned} C_{peff} &= C_p + Q_L \left(\frac{\partial M}{\partial T} \right)_P \\ \alpha_{eff} &= \alpha + \rho \frac{Q_L}{T} \left(\frac{\partial M}{\partial T} \right)_T \end{aligned} \quad (11)$$

where C_p is the heat capacity of the solid crust; Q_L is the latent heat of melting of the crust.

3. Model setup

We use a large-scale model domain (4000×670 km) to study the dynamics of craton thinning and destruction controlled by the interaction between subduction and the MLD layer (Fig. 2). Non-uniform rectangular numerical grid is designed with a resolution varying from 2×2 km in the area of interest gradually changed to 30×30 km at the margins. The initial model configuration includes an oceanic plate and a continental plate, separated by a low-viscosity weak zone to

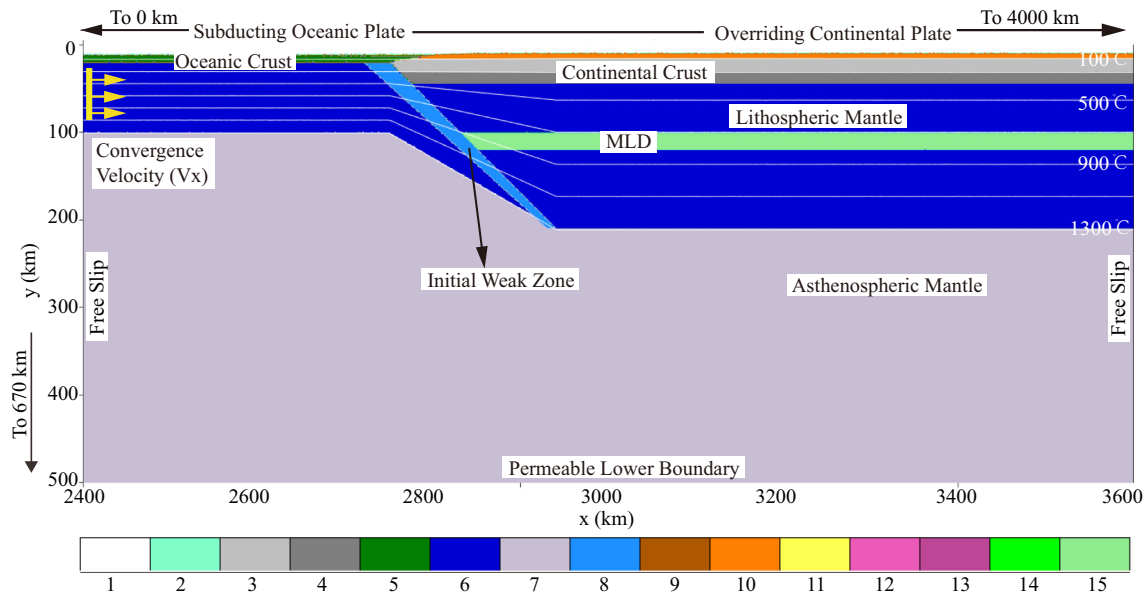


Fig. 2. Initial configuration of the numerical model. Model size is 4000×670 km. White lines are isotherms in $^{\circ}\text{C}$. Colors indicate the rock types, specified by 1, air; 2, water; 3, upper continental crust; 4, lower continental crust; 5, oceanic crust; 6, lithosphere mantle; 7, asthenosphere mantle; 8, hydrated mantle (i.e., initial weak zone); 9–10, sediment; 11, partial molten sediment; 12, partial molten upper continental crust; 13, partial molten lower continental crust; 14, partial molten oceanic crust; 15, mid-lithosphere discontinuity (MLD) layer.

initiate subduction. The oceanic lithosphere is represented by an 8-km mafic crust, and a mantle layer with a thickness depending on the age of the lithosphere. The initial continental lithosphere is composed of a 20-km thick felsic upper crust, a 15-km thick mafic lower crust, and a mantle layer of anhydrous peridotite with variable thicknesses. Detailed flow laws and properties of variable lithologies are described in Tables 1 and 2, respectively.

Within the cratonic lithosphere, a MLD layer is prescribed, with the initial thickness of 20 km at a depth of 90 km in the reference model, the effects of which were systematically tested. Since the rheological properties of the MLD layer have not been determined so far, we have also tested variable rheology of this layer. By seismic observations, it is generally regarded as a relatively weaker layer comparing to both the overlying and underlying lithospheric mantle since it has a lower seismic velocity (Dawson and Smith, 1977, 1988; Lu et al., 1991; Griffin et al., 1999a, 2004; Gao et al., 2002; Downes et al., 2004; Tang et al., 2013). In this study, we apply either constant viscosity or wet olivine rheology for the MLD layer (Ranalli, 1995).

The topography is calculated dynamically as an internal free surface by using a low-viscosity layer above the upper crust, i.e. ‘sticky air’ (Schmelting et al., 2008). Based on the isostatic principle, the thickness of sticky air layer was set as 10 km above the continental crust and 12 km above the oceanic crust.

The thermal boundary conditions are fixed with 0°C and 1600°C for the upper and lower boundaries, respectively. For the oceanic plate, the initial thermal structure is defined by the half-space cooling model and

is controlled by its age (Turcotte and Schubert, 2002). For the continental plate, the initial thermal structure is a linear interpolation with 0°C at the surface and 1350°C at the bottom of the lithosphere. An adiabatic thermal gradient of $0.5^{\circ}\text{C}/\text{km}$ is applied for the asthenosphere.

The velocity boundary conditions are free slip at all boundaries except the permeable lower boundary, which is imposed with an infinity-like mass-conservative condition (e.g., Li et al., 2010, 2016). The subducting plate is pushed toward the continent with a constant convergence velocity (V_x). The velocity can be attributed to the combination of three major forces of subduction, i.e., ridge push, convection drag and slab pull.

4. Results

4.1. General model without MLD

We firstly present a model without the MLD layer that is similar to that in Shi et al. (2019). In this model, the age of subducting oceanic lithosphere is set to be 60 Ma, with the oceanic crustal thickness of 8 km. For the continental lithosphere, the thickness is fixed to 200 km, which is estimated as the original lithospheric thickness of North China Craton (Carlson et al., 2005; Zhu et al., 2012). The initial angle of subduction is set to 45° , with a prescribed constant convergence velocity of 5 cm/yr. In this experiment, the reference density contrast (i.e. at the same pressure and temperature) between the lithospheric and asthenospheric mantle is zero.

Table 1
Viscous flow laws used in the numerical experiments^a.

Symbol	Flow law	E (kJ mol^{-1})	V ($\text{J MPa}^{-1} \text{mol}^{-1}$)	n	A_D ($\text{MPa}^{-n} \text{s}^{-1}$)	η_0 ($\text{Pa}^n \text{s}$)
A	Wet quartzite	154	8	2.3	3.2×10^{-4}	1.97×10^{17}
B	Plagioclase	238	8	3.2	3.3×10^{-4}	4.80×10^{22}
C	Dry olivine	532	8	3.5	2.5×10^4	3.98×10^{16}
D	Wet olivine	470	8	4.0	2.0×10^3	5.00×10^{20}
E	Molten felsic	0	0	1.0	2.0×10^{-9}	5.00×10^{14}
F	Molten mafic	0	0	1.0	1.0×10^{-7}	1.00×10^{13}

^a References are from Kirby (1983), Kirby and Kronenberg (1987), Ranalli and Murphy (1987), Ji and Zhao (1993), Ranalli (1995), and Karato and Jung (2003).

Table 2
Materials properties used in the numerical experiments.

Material	State	ρ_0 (kg m ⁻³)	k^a (Wm ⁻¹ K ⁻¹)	T_{solidus}^b (K)	T_{liquidus}^b (K)	Q_L (kJ kg ⁻¹)	H_r ($\mu\text{W m}^{-3}$)	Viscous flow law ^c	Plastic ^d $\sin(\varphi_{\text{eff}})$
Sediment	Solid	2700	K1	TS1	TL1	300	2.0	A	0.15
	Molten	2500	K1	TS1	TL1	300	2.0	E	0.06
Oceanic crust	Solid	3000	K2	TS2	TL2	380	0.25	B	0.15
	Molten	2900	K2	TS2	TL2	380	0.25	F	0.06
Continental upper crust	Solid	2700	K1	TS1	TL1	300	2.0	A	0.15
	Molten	2500	K1	TS1	TL1	300	2.0	E	0.06
Continental lower crust	Solid	3000	K1	TS2	TL2	380	0.5	B	0.15
	Molten	2500	K1	TS2	TL2	380	0.5	E	0.06
Mantle	Dry	3300	K3	-	-	-	0.022	C	0.60
	Hydrated	3200	K3	-	-	-	0.022	D	0.06
	MLD ^e	3300	K3	-	-	-	0.022	D	0.06
References ^f	-	1, 2	3	4	4	1, 2	1	-	-

^a $K1 = [0.64 + 807/(T + 77)] \exp(0.00004^*P)$; $K2 = [1.18 + 474/(T + 77)] \exp(0.00004^*P)$; $K3 = [0.73 + 1293/(T + 77)] \exp(0.00004^*P)$.
^b $TS1 = 889 + 17,900/(P + 54) + 20,200/(P + 54)^2$, at $P < 1200$ MPa; or $831 + 0.06P$, at $P > 1200$ MPa. $TL1 = 1262 + 0.09P$; $TS2 = 973 - 70,400/(P + 354) + 778 \times 10^5/(P + 354)^2$, at $P < 1600$ MPa; or $935 + 0.0035P + 0.0000062P^2$, at $P > 1600$ MPa. $TL2 = 1423 + 0.105P$.
^c Parameters of viscous flow laws are shown in Table 1.
^d The plastic cohesion is zero in all the experiments. φ_{eff} is the effective internal frictional angle implemented for plastic rheology.
^e MLD stands for the properties of the mid-lithosphere discontinuity (MLD) layer.
^f 1 = (Turcotte and Schubert, 2002); 2 = (Bittner and Schmeling, 1995); 3 = (Clauser and Huenges, 1995); 4 = (Schmidt and Poli, 1998).

The evolutions of material and viscosity fields are shown in Fig. 3. The subducting slab carries sediments and crust into the mantle, which leads to significant partial melting at the bottom of the subduction channel. Due to the low density, melt-bearing sedimentary materials migrate sub-horizontally in the lower portion of overriding cratonic lithosphere. The channel length is only ~100 km at the model time of 21.5 Myrs (Fig. 3a) and extended to ~400 km at 50.2 Myrs (Fig. 3d), leading to the foundering of the bottom ~50 km of the lithosphere that is rheologically weak. However, the extent of the destruction of craton lithosphere is much smaller compared to observations of NCC (e.g., Zhu et al., 2012), which indicates that it is difficult for

such kind of simple subduction process to significantly destruct the overriding craton.

4.2. Reference model with MLD

In this model, a MLD layer is set up with a thickness of 20 km, a depth of 90 km and a constant viscosity of $\eta_c = 10^{20}$ Pa·s. During subduction, a significant amount of sedimentary rocks are carried deep into the subduction channel. The partial melting and return flow erode the lower lithospheric mantle of the overriding craton (Fig. 4a–b and 4a’–b’), which finally lead to the connection between the upwelling hot

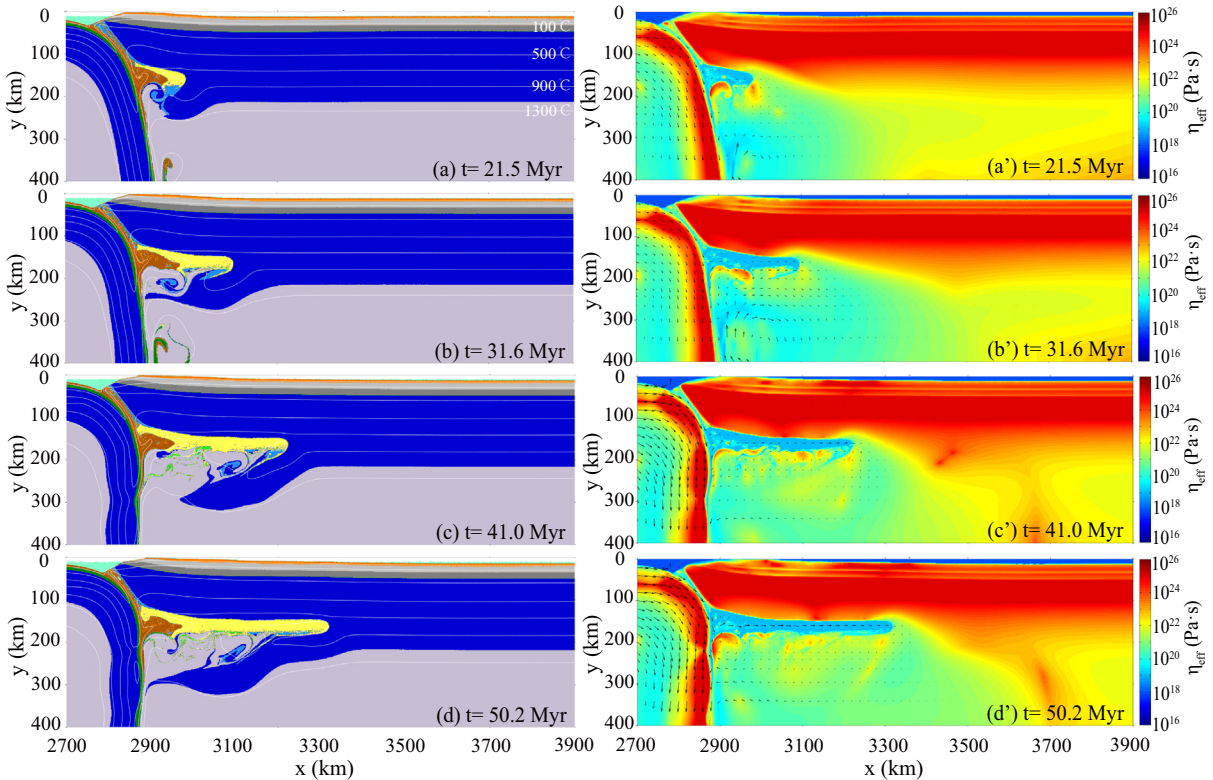


Fig. 3. Evolution of the model without the MLD layer. The colors show the evolution of material field (a-d) and the viscosity structure (a'-d'). White lines in Fig. 3a–d are the temperature isotherms. Black arrows in Fig. 3a'–d' represent the velocity vector. η_{eff} is the effective viscosity. Time (Myr) of model evolution (t) is given in each panel.

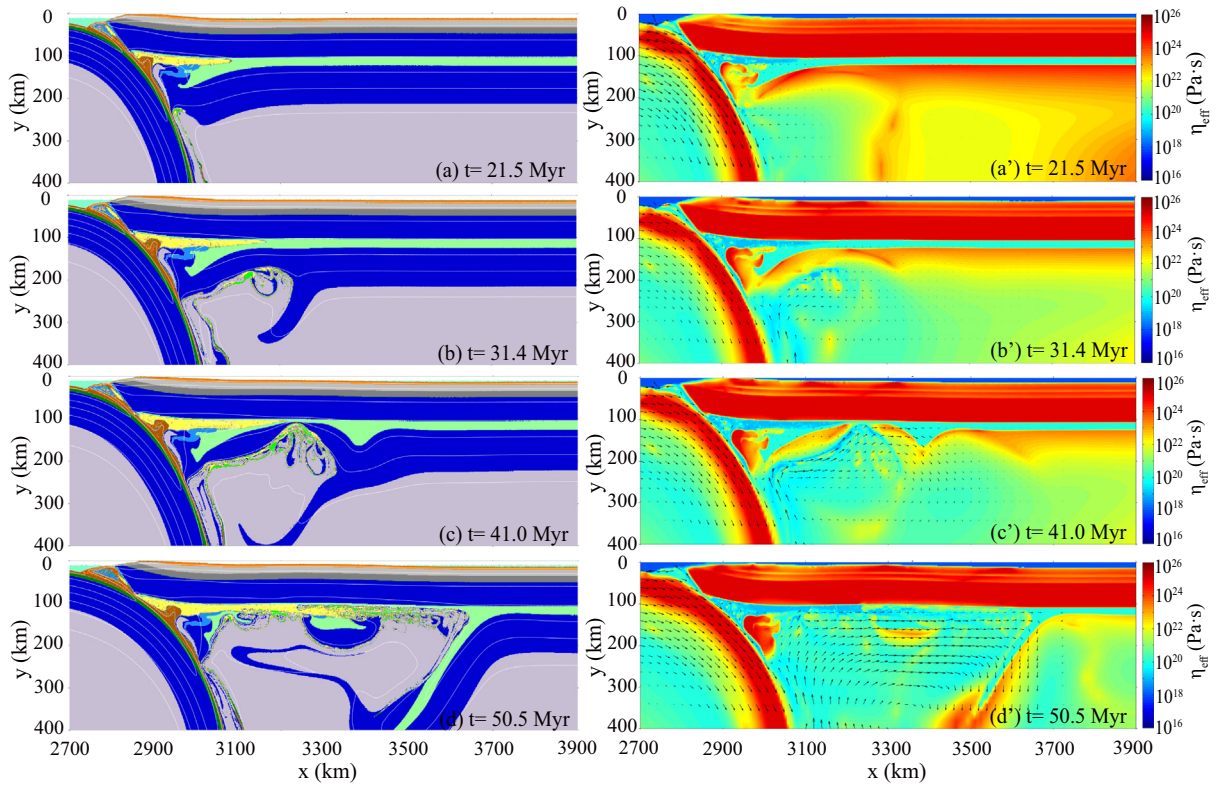


Fig. 4. Evolution of the reference model. Thickness of the MLD layer (H) is 20 km. Depth of MLD layer (D) is 90 km. Viscosity of MLD layer (η_c) is 10^{20} Pa·s. Colors and symbols are the same as in Fig. 3.

asthenosphere and the weak MLD layer at 41.0 Myrs (Fig. 4c and c'). Thus the favorable condition of delamination (Bird, 1979; Lei et al., 2019) is obtained, which finally contributes to the total removal of the lower lithosphere beneath the MLD layer. At the model time of 50.5 Myrs, extensive thinning and destruction of cratonic lithosphere occur under the interaction between the subduction and MLD (Fig. 4d and d'). The extent of total thinning is approximately 700 km horizontally and 100 km vertically, which is considerably larger than that without the MLD layer (c.f. Fig. 3d and d'). Moreover, unlike the model without the MLD in which the destruction is limited to the mantle wedge that requires continuous spread of the melt-bearing sedimentary channel, the delamination of the lithosphere beneath the MLD could propagate along the MLD layer without the spreading of the melt-bearing sedimentary channel once started (Bird, 1979, Liu et al., 2018a, 2018b).

Furthermore, in order to illustrate the mechanisms of cratonic destruction, we perform three additional series of experiments. One series is focusing on the properties of the MLD layer (Section 4.3), another series on different subduction conditions (Section 4.4), and the third series on the reference density contrast between the lithospheric and asthenospheric mantle, as well as the lithosphere viscosity (Section 4.5).

4.3. Effects of the MLD properties

4.3.1. Influence of the MLD layer thickness

The thickness of MLD layer was generally suggested as ~20–40 km, which might significantly affect the thinning and destruction of cratonic lithosphere (Abt et al., 2010; Chen et al., 2014; Hopper et al., 2014; Liu et al., 2018a). In this section, two additional numerical experiments are conducted with a MLD thickness of 10 km (Fig. 5a) and 40 km

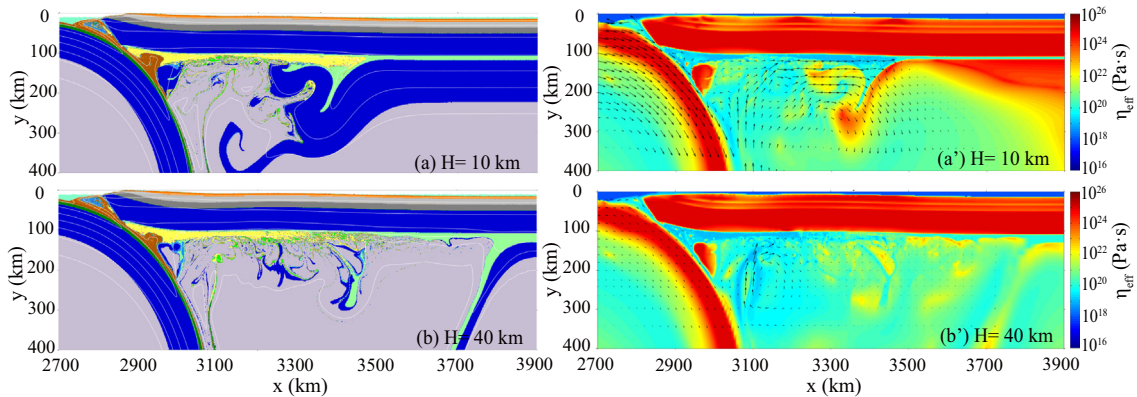


Fig. 5. Representative snapshots of experiments with different thicknesses of MLD layer (H): (a) $H = 10$ km; (b) $H = 40$ km. Other parameters are identical to the reference model. Colors and symbols are the same as in Fig. 3. The same time of model evolution is applied as 50 Myrs.

(Fig. 5b), respectively. Other parameters are identical to the reference model, which has a 20-km thick MLD layer (Fig. 4d).

A thinner MLD layer of 10 km results in significantly slower destruction and narrower thinned region at the same model time of 50 Myrs compared to the reference model (c.f. Figs. 4d and 5a). However, a thicker MLD of 40 km leads to significantly faster destruction of the craton lithosphere, with a horizontal extent of 800 km at 50 Myrs (Fig. 5b).

4.3.2. Influence of the MLD layer depth

Another two experiments were performed to test the influence of the MLD layer at a depth of 80 km (Fig. 6a) and 100 km (Fig. 6b), respectively. The other parameters are kept the same as those of the reference model (Fig. 4d). With a shallower MLD at 80 km (Fig. 6a), the subduction-induced partial molten materials couldn't connect the hot asthenosphere to the weak MLD layer. Therefore, the delamination of the lithospheric root does not occur. In contrast, with a MLD at 100 km depth (Fig. 6b), the subduction-induced partial melting can easily erode the bottom of overriding lithosphere, which helps to connect the arising asthenosphere with the MLD that leads to the peel-off of the bottom part of the lithosphere. The results here suggest that the depth of the MLD is an important factor in controlling craton stability.

4.3.3. Influence of the MLD layer strength

In addition to its thickness and depth, we also investigated the role of rheological strength of the MLD layer. To do so, we constructed two sets of experiments (Figs. 7 and 8). In the first set, constant viscosities (η_c) between 10^{18} Pa·s and 10^{23} Pa·s are used (Fig. 7). While in the second set of experiments (Fig. 8), the power-law rheology (as in Section 2.2) is applied for the MLD layer, with pre-exponential viscous factor (η_0) varying between 10^{12} Paⁿ·s and 10^{22} Paⁿ·s (Fig. 8). The numerical results indicate that the cratonic lithosphere could be easily destructed with a lower MLD strength in both sets of numerical models (Figs. 7a and 8a–c). Meanwhile, the weaker the MLD layer is, the faster the thinning and destruction process undergoes. In the case of a relatively strong MLD layer ($\eta_c = 10^{22}$ Pa·s or $\eta_0 = 10^{22}$ Paⁿ·s), although the connection between the asthenosphere and the MLD is still present, there is, however, no large-scale peel-off of the lower lithospheric layer, resulting in a limited destruction that is similar to the model without the MLD (c.f. Figs. 4d, 7b and 8d).

4.4. Effects of subduction conditions

In this section, we investigate the sensitivity of lithospheric destruction to various subduction related parameters, such as the age of oceanic lithosphere, the thickness of oceanic crust, the convergence rate and the initial subduction angle (Gerya and Meilick, 2011; Qiao et al., 2012,

2013; He, 2014; Wang Z et al., 2016; Cheng et al., 2016; Cheng and Huang, 2017; Shi et al., 2019).

4.4.1. Influence of the age of oceanic lithosphere

Fig. 9 shows the model results with different ages of the oceanic lithosphere, varying from 20 to 100 Ma. In the model with very young oceanic lithosphere of 20 Ma, the flat subduction is induced, which prevents the delamination process because of the strong coupling between the subducting and overlying plates (Fig. 9a; e.g., Huangfu et al., 2016). In all the other cases, the subduction generates enough partial molten materials that eroded the lower layer of overriding lithosphere and forms a pathway for the uprising asthenosphere to reach the weak MLD layer, which thus lead to the delamination of the entire lower lithosphere (Fig. 9b–c). The extents of lithospheric destruction in Fig. 9b–c are around 700 km and 100 km in horizontal and vertical direction, respectively, which are almost the same as the results based on the reference model (Fig. 4d).

4.4.2. Influence of the oceanic crustal thickness

The thickness of a normal oceanic crust is generally 6–8 km (White et al., 1992); however, an oceanic plateau can have a much thicker crust. Thus, we created a series of models that have an oceanic crust with a thickness varying from 4 km to 12 km (Fig. 10). The results are shown in Fig. 10, which indicates that with the thickness of oceanic crust increasing from 4 km to 12 km, the partial melting and weak materials originated from the subduction channel extended faster and further along the MLD layer, leading to a wider range of thinning and destruction of cratonic lithosphere. For example, the horizontal extent of craton destruction is only ~200 km with a 4-km thick oceanic crust (Fig. 10a and a') but reaches ~800 km with a 12-km thick oceanic crust (Fig. 10b and b'). We also performed several experiments with the varying thickness of the sedimentary layer, which show similar results (Fig. S1). The horizontal extent of destruction increases from 200 km with 2-km thick sediment layer (Fig. S1a) to 800 km with an 8-km thick sediment layer (Fig. S1c).

4.4.3. Influence of convergence rate

Convergence velocity controls the thermal structure and partial melting in the subduction channel (Liu et al., 2017), which could affect the weakening of overriding lithosphere as well as the possible connection between arising asthenosphere and the MLD layer. In the models presented so far, we imposed the constant convergence velocity of $V_x = 5$ cm/yr. In order to understand its influence, we further constructed two additional experiments with convergence velocity of 2 and 8 cm/yr, respectively.

The destruction rate of the craton lithosphere is positively correlated to the convergence velocity. When the convergence velocity is 2 cm/yr,

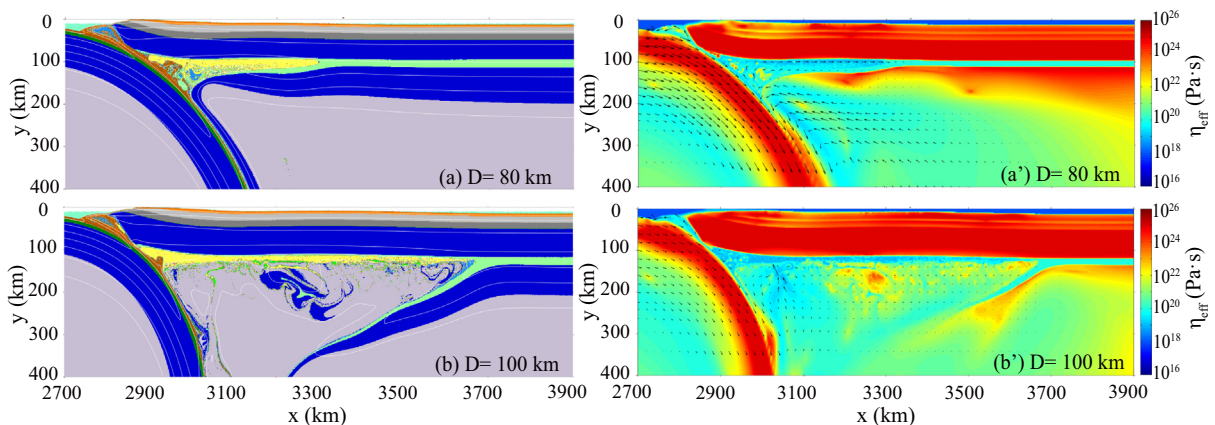


Fig. 6. Representative snapshots of experiments with various depths of MLD layer (D): (a) $D = 80$ km; (b) $D = 100$ km. Other parameters are identical to the reference model with $D = 90$ km. Colors and symbols are the same as in Fig. 3. The same time of model evolution is applied as 50 Myrs.

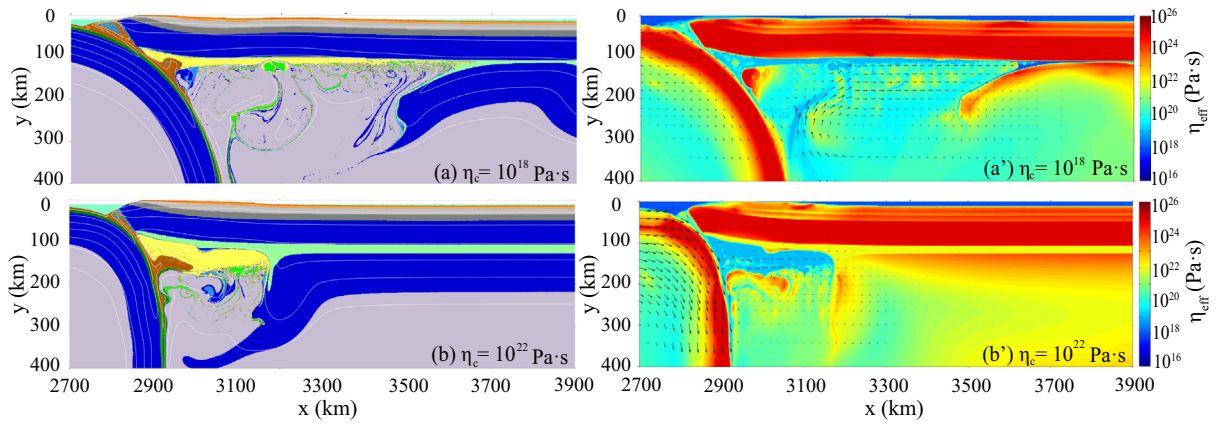


Fig. 7. Representative snapshots of experiments with various constant viscosities of MLD layer (η_c): (a) $\eta_c = 10^{18}$ Pa·s; (b) $\eta_c = 10^{22}$ Pa·s. Other parameters are identical to the reference model. Colors and symbols are the same as in Fig. 3. The same time of model evolution is applied as 50 Myrs.

the lithospheric mantle beneath the MLD layer is just penetrated by the hot partially molten upwelling at 125 Myrs, which is much slower than the reference model (Fig. 4a and 11a). However, in the case of $V_x = 8$ cm/yr, the lower-layer lithosphere is totally peeled off up to 500 km horizontally at 32 Myrs (Fig. 11b).

4.4.4. Influence of the initial subduction angle

The coupling of converging plates is directly affected by the initial subduction angle (Li et al., 2011; Huangfu et al., 2016). Two additional experiments are conducted with the initial dip angle of weak zone to be 30° and 60° , respectively, in comparison to the reference model of 45° . The results are shown in Fig. 12, which indicates that the initial dip angle can also influence the extent and rate of craton destruction, although it is not the first-order controlling factor. Subduction with a

small dipping angle appears to be able to reduce the temperature in the mantle wedge, such that not enough partial melts are generated to erode a wide range of the overriding craton (Fig. 12a). On the other hand, when the angle increases, the subduction produces sufficient amount of melts and weak materials that can trigger the delamination process (Fig. 12b).

4.5. Effects of density contrast across the LAB and lithosphere viscosity

A positive reference density contrast between the lithospheric and asthenospheric mantle is regarded as one of the most important driving forces for the thinning and destruction of the cratonic lithosphere (Li et al., 2016). But generally, the reference density (i.e. at the same pressure and temperature) of the continental lithospheric mantle is lower

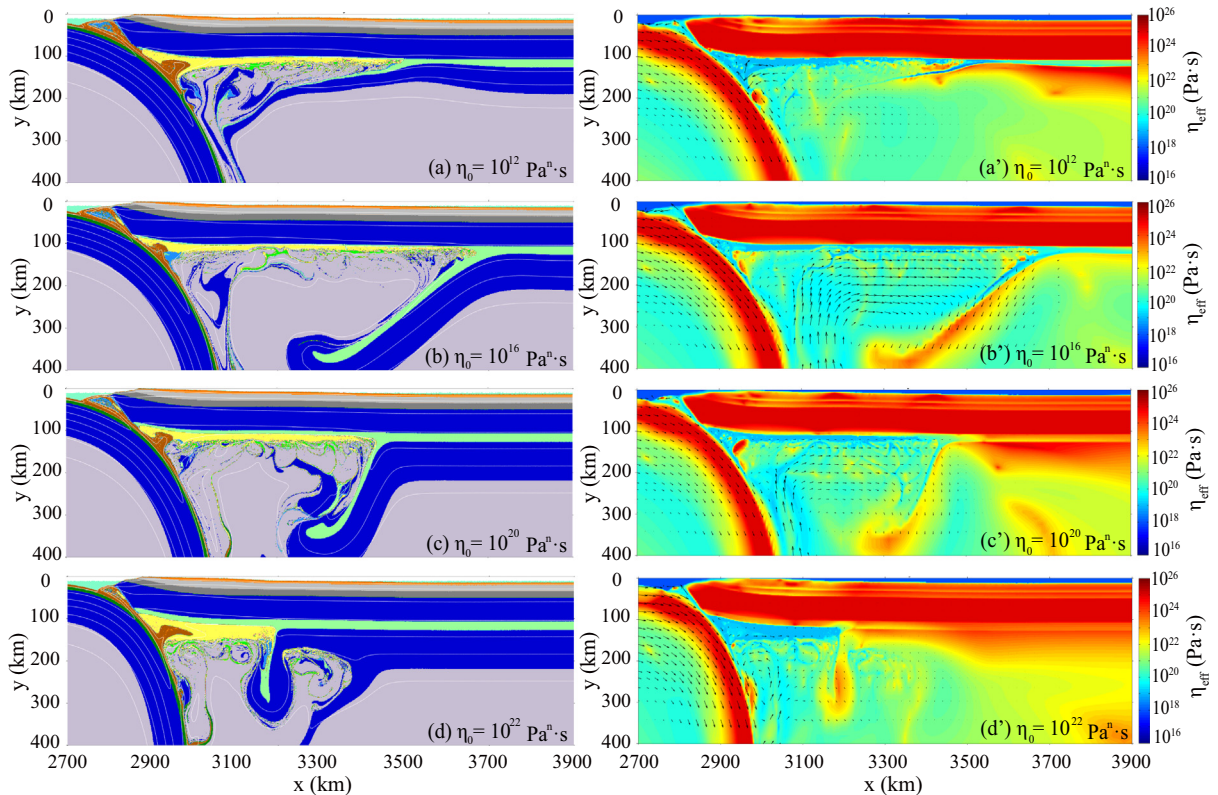


Fig. 8. Representative snapshots of experiments with various pre-exponential viscous factors of MLD layer (η_0) at -50 Myrs: (a) $\eta_0 = 10^{12}$ Paⁿ·s; (b) $\eta_0 = 10^{16}$ Paⁿ·s; (c) $\eta_0 = 10^{20}$ Paⁿ·s; (d) $\eta_0 = 10^{22}$ Paⁿ·s. Other parameters are identical to the reference model. Colors and symbols are the same as in Fig. 3. The same time of model evolution is applied as 50 Myrs.

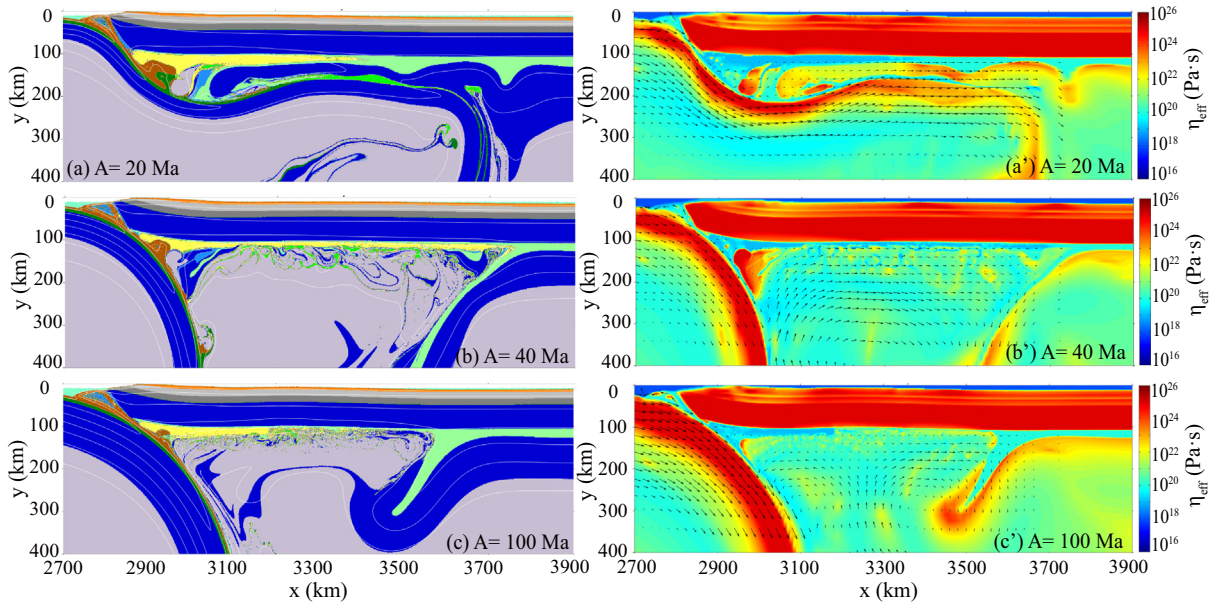


Fig. 9. Representative snapshots of experiments with various ages (A) of oceanic lithosphere: (a) $A = 20$ Ma; (b) $A = 40$ Ma; (c) $A = 100$ Ma. Other parameters are identical to the reference model. Colors and symbols are the same as in Fig. 3. The same time of model evolution is applied as 50 Myrs.

than that of asthenosphere (Djomani et al., 2001; Schutt and Lesher, 2006). However, the continental lithospheric density could be increased by eclogitized magmatic intrusions (dykes) from ancient plumes (Sobolev et al., 2011), which results in compositionally dense lithospheric mantle (e.g., pyroxenite), in comparison to the underlain peridotite (Jull and Kelemen, 2001; Lee et al., 2006, 2011). Therefore, a positive reference density contrast between the lithospheric mantle and asthenosphere may be obtained from the rejuvenation of depleted continental lithosphere by metasomatic plume or subduction-induced processes. In this section, we construct two additional sets of experiments with either negative (Fig. 13a and b) or positive (Fig. 13c and d) reference density contrast across the LAB.

The experimental results show that no significant thinning and destruction can happen (Fig. 13a), if the density of the lithospheric mantle is much lower than that of the asthenosphere ($\Delta\rho = -40$ kg/m³). However, unlike the previous studies without the MLD layer (Shi et al., 2019), the lithospheric mantle under the MLD layer can be destroyed in a narrow region with a less negative reference density contrast across the LAB ($\Delta\rho = -30$ kg/m³) (Fig. 13b). Furthermore, as shown in Fig. 13c and d, the rate and extent of the thinning and destruction are

larger with increasing values of the reference density contrast. A large-scale destruction of the cratonic lithosphere occurred when the reference density contrast is positive, in which the horizontal destruction range extends as large as 700 km with $\Delta\rho$ of 30 kg/m³ at 50 Myrs (Fig. 13c) and 900 km with $\Delta\rho$ of 40 kg/m³ at 50 Myrs.

We also varied the viscosity of lithospheric mantle by either increasing or decreasing its pre-exponential viscous factor (η_0) by 100 times. The experiments show limited lithosphere thinning with higher viscosity (Fig. S2a), but larger extent of delamination with lower viscosity (Fig. S2b) compared to the reference model (Fig. 4d).

5. Discussion

5.1. Role of subduction and MLD on craton destruction

Our numerical experiments indicate that the thinning and destruction of cratonic lithospheric mantle could be attributed to the interaction between the subduction and the weak MLD layer. In the subduction regime, partial molten material occurs along the subducting oceanic plate, migrates upwards, and erodes the bottom of the cratonic

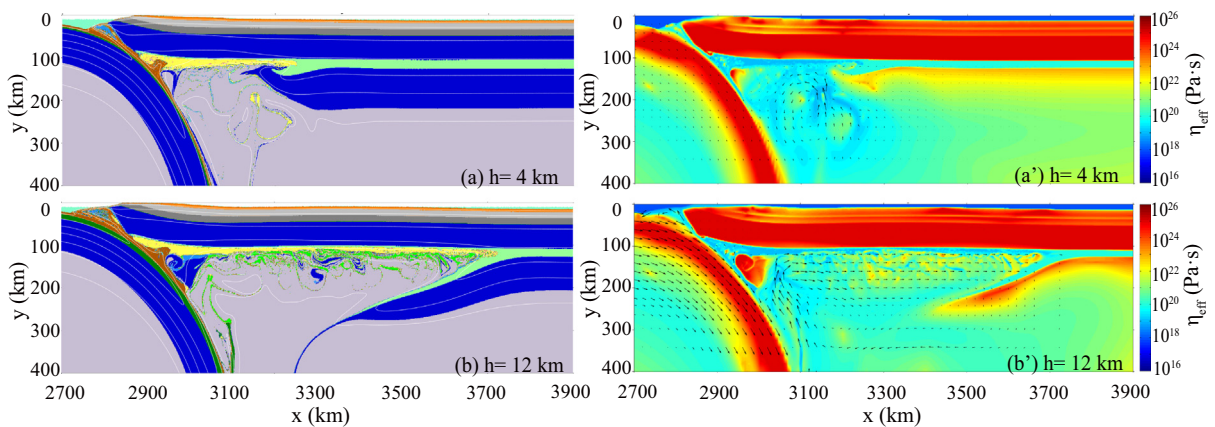


Fig. 10. Representative snapshots of experiments with various thicknesses of oceanic crust (h): (a) $h = 4$ km; (b) $h = 12$ km. Other parameters are identical to the reference model. Colors and symbols are the same as in Fig. 3. The same time of model evolution is applied as 50 Myrs.

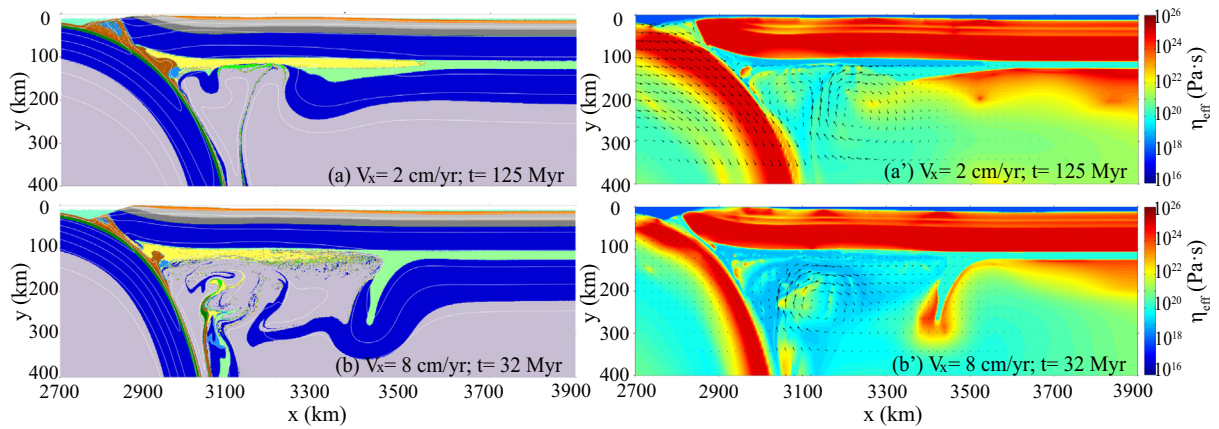


Fig. 11. Representative snapshots of experiments with various convergence velocities (V_x): (a) $V_x = 2$ cm/yr; (b) $V_x = 8$ cm/yr. The time of subduction (t): (a) $t = 125$ Myr; (b) $t = 32$ Myr, which indicate the same length of subduction. Other parameters are identical to the reference model. Colors and symbols are the same as in Fig. 3. The same time of model evolution is applied as 50 Myrs.

lithospheric mantle under small-scale mantle convection (Menzies and Xu, 1998; Arcay et al., 2005; Wu et al., 2008; Xu et al., 2008; Zhu et al., 2012; He, 2014; Li et al., 2015, 2019; Liu et al., 2017). The dynamics of cratonic lithospheric thinning induced by oceanic plate subduction has been investigated in Shi et al. (2019) and also in our model without the MLD layer (Fig. 3). Both experiments showed that the extent of horizontal erosion and vertical thinning, triggered by the erosion of the partial molten material, could be about 400 km and 50–70 km, respectively, which is less than that of the eastern North China Craton with values of >600 km horizontally and 100 km vertically (Xu et al., 2009; Zhu and Zheng, 2009). It indicates that the subduction-induced perturbation and erosion are generally slow for large-scale destruction of the thick cratonic lithosphere, which thus requires other additional mechanisms.

The existence of a weak MLD layer can decouple the overlying and underlying lithospheric mantle layers (Liu et al., 2018a; Wang et al., 2018). As far as the MLD layer comes in direct contact with the asthenosphere, the cratonic lithosphere will be unstable. The importance of a weak MLD layer on the thinning and destruction of the cratonic lithosphere has been investigated in several numerical studies (Liao and Gerya, 2014; Wang et al., 2018; Liu et al., 2018a, 2018b). Liao and Gerya (2014) proposed that the existence of a weak MLD layer could enhance the deformation of the overlying cratonic lithosphere under cratonic extension and rifting setting. In addition, Wang et al. (2018, 2017) showed that the cratonic lithosphere can be decoupled from the upper lithosphere and recoupled with the drifted oceanic lithosphere during continental drifting owing to the weak MLD layer. Moreover, the edge

failure of the weak MLD layer could result in rapid delamination of the underlying cratonic lithosphere (Liu et al., 2018a, 2018b).

In the previous models with MLD-induced cratonic destruction, the MLD layer is generally exposed to the neighboring asthenosphere (Wang et al., 2018; Liu et al., 2018a, 2018b), which implies that the neighboring lithosphere is rather thin. In such cases, the delamination along MLD layer is a purely gravity-driven process. These models also indicate that if the MLD layer is not connected with the weak asthenosphere, the cratonic lithosphere will be stable without delamination. In the current study, we propose that the subduction can play as a trigger, during which the partial melting weakens the bottom of the lithosphere and finally connect the MLD layer with the asthenosphere (Fig. 4). Thus the typical environment of delamination (Bird, 1979; Lei et al., 2019) is reached, which finally leads to the thinning and destruction of cratonic lithosphere.

The whole processes from subduction to lithospheric weakening and craton destruction are affected by a number of factors, e.g., (a) properties of MLD layer; (b) subduction conditions; and (c) density contrast between the lithospheric mantle and asthenosphere. For the MLD layer, its thickness, depth and viscosity can play significant roles on craton thinning and destruction. Specifically, the destruction ranges of cratonic lithosphere increase from 300 km to as large as 800 km with the thickness of MLD layer varying from 10 km to 40 km (Fig. 5). The upwelling tunnel and the connection between the MLD layer and asthenosphere can be easily established with a thick or deeply located MLD layer (Figs. 5b and 6b), resulting in a great amount of partial melts and weak materials penetrating

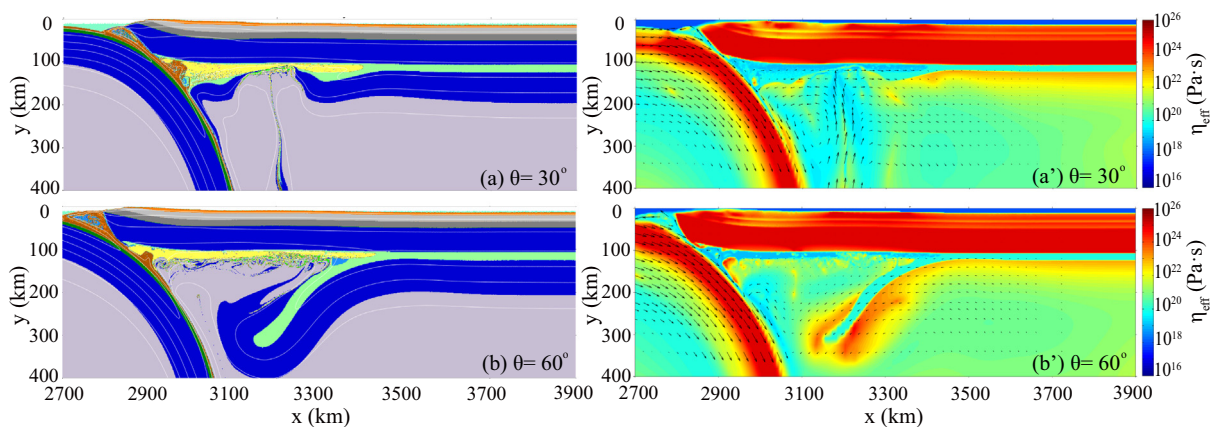


Fig. 12. Representative snapshots of experiments with various initial dip angles of the weak zone (θ): (a) $\theta = 30^\circ$; (b) $\theta = 60^\circ$. Other parameters are identical to the reference model. Colors and symbols are the same as in Fig. 3. The same time of model evolution is applied as 50 Myrs.

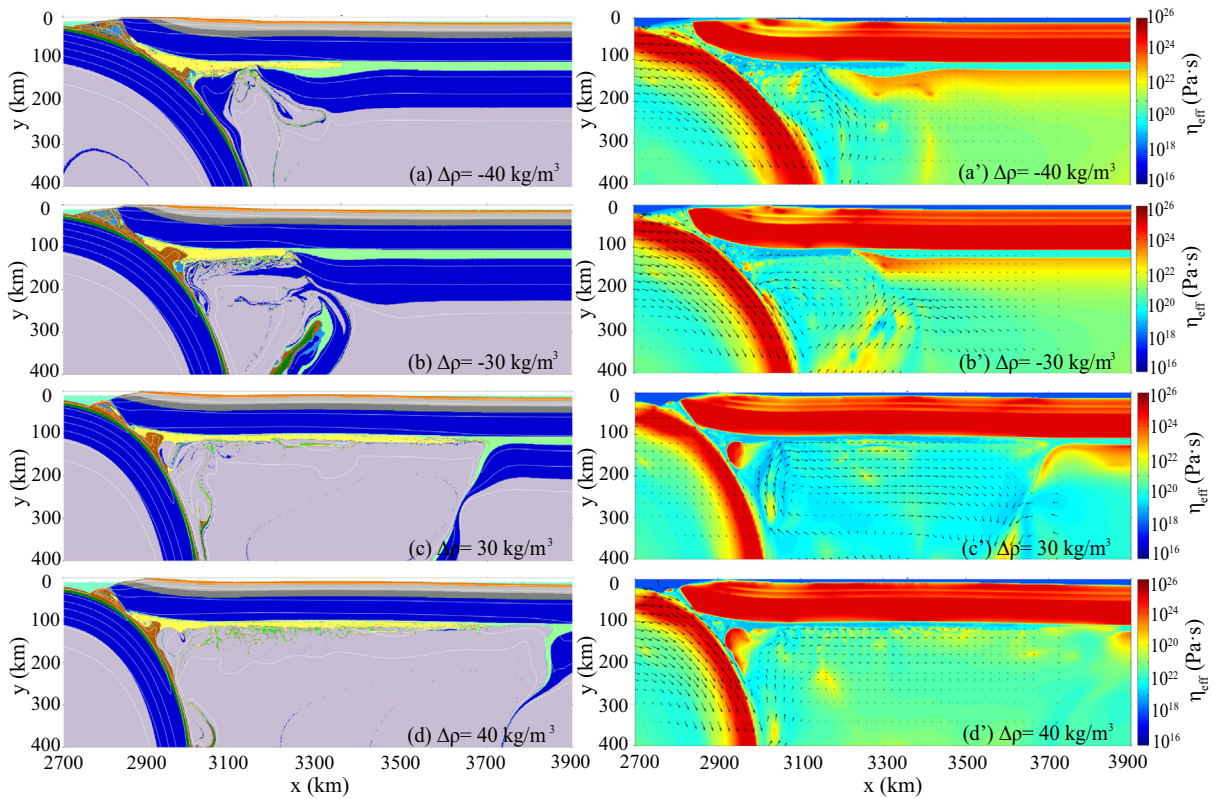


Fig. 13. Representative snapshots of experiments with various reference density contrast between the lithospheric mantle and asthenosphere ($\Delta\rho = \rho_{\text{lith}} - \rho_{\text{asth}}$): (a) $\Delta\rho = -40 \text{ kg/m}^3$; (b) $\Delta\rho = -30 \text{ kg/m}^3$; (c) $\Delta\rho = 30 \text{ kg/m}^3$; (d) $\Delta\rho = 40 \text{ kg/m}^3$. Other parameters are identical to the reference model. Colors and symbols are the same as in Fig. 3. The same time of model evolution is applied as 50 Myrs.

through the MLD layer, which eventually determines the large scale destruction of cratonic lithosphere. In addition, we note that the cratonic lithosphere can be only extensively destroyed with a relatively low viscosity ($\eta_c < 10^{22} \text{ Pa}\cdot\text{s}$ or $\eta_o < 10^{22} \text{ Pa}\cdot\text{s}$) of the MLD layer (Figs. 7 and 8). If the MLD layer of stable cratons is not weak enough for decoupling, thus no connection between the MLD layer and the asthenosphere can be established, craton destruction may not occur. This is consistent with previous studies that have shown that most cratons on Earth are stable and still have a thick cratonic lithosphere (Artemieva, 2009). However, the MLD layer was likely weak enough in the eastern NCC. Thus, the cratonic lithosphere of the eastern NCC was destroyed and removed along the MLD layer (Chen et al., 2014; Wang et al., 2018).

For the properties of subduction, the thickness of oceanic crust, convergence velocity and the initial subduction angle can affect the thinning and destruction of the cratonic lithosphere dramatically. Our numerical results show that the craton destruction are favored by thick oceanic crust, high convergence velocity and relatively high initial subduction angle (Figs. 10, 11, and 12), which contribute to the establishment of the connection between the MLD layer and the asthenosphere, thus leading to the thinning and destruction of the cratonic lithosphere. However, the age of subducting oceanic lithosphere has little impact on craton thinning and destruction except when the slab is very young (e.g., 20 Ma) (Fig. 9) that leads to flat subduction and exhibits another mechanism of craton destruction (Liu and Li, 2018). It indicates that only if subduction can play as a trigger and the connection between the MLD layer and the asthenosphere can be established, significant craton destruction will occur. Furthermore, it has to be mentioned that the thinning and destruction of the cratonic lithosphere can occur with the density contrast between the lithospheric mantle and the asthenosphere larger than -30 kg/m^3 . Meanwhile, the larger the density contrast is, the wider destruction extent of the cratonic lithosphere will be (Fig. 13).

5.2. Geological implications for the North China Craton (NCC)

The NCC has undergone the most excessive destruction comparing to other global Precambrian cratons since the Mesozoic. Although the mechanisms are still under debate (Menzies et al., 2007), extensive studies and great progresses have been made to understand them (Griffin et al., 1998; Menzies and Xu, 1998; Xu, 2001; Gao et al., 2002; Zhang et al., 2002; Yang et al., 2003; Chen et al., 2004; Xu et al., 2008; Chen et al., 2014; Wu et al., 2014; Liu and Li, 2018). The western NCC is relatively stable, whereas the eastern NCC underwent strong tectono-magmatic activity and experienced significant thinning and destruction in the Mesozoic (Gao et al., 2002; Zhang et al., 2003; Zhai et al., 2004; Zhai, 2008).

Recent seismic studies have proved a strong velocity drop at $\sim 100 \text{ km}$ depth beneath the eastern NCC (e.g., Fischer et al., 2010), where a thick cratonic mantle extending to $\sim 200 \text{ km}$ depth is expected (e.g., Chen CW et al., 2009). The thinning of the eastern NCC could be $50\text{--}70 \text{ km}$ with models only induced by oceanic plate subduction (Fig. 3; Shi et al., 2019), showing that the Paleo-Pacific subduction can be a key triggering mechanism for the thinning and destruction of the eastern NCC. In addition, we suggest that the MLD layer existed in the eastern NCC with a depth of ~ 80 to 100 km , could be another significant contribution on its thinning and destruction. The alkaline magmatism (e.g., syenites) occurred in the eastern NCC from pre-Mesozoic to early Mesozoic could provide a good evidence. Yang et al. (2012) proposed that these alkaline rocks are enriched in large ion lithophile elements and light rare earth elements and depleted in high field strength elements, indicating that they were derived from a refractory lithospheric mantle. Furthermore, O'Reilly and Griffin (2010) suggested that metasomatically enriched elements appeared at $\sim 100 \text{ km}$ depth in the cratonic lithosphere, suggesting that a MLD layer or metasomatism existed at $\sim 100 \text{ km}$ depth within the lithospheric mantle of the eastern NCC before its thinning and destruction. Our numerical models (Fig. 4d)

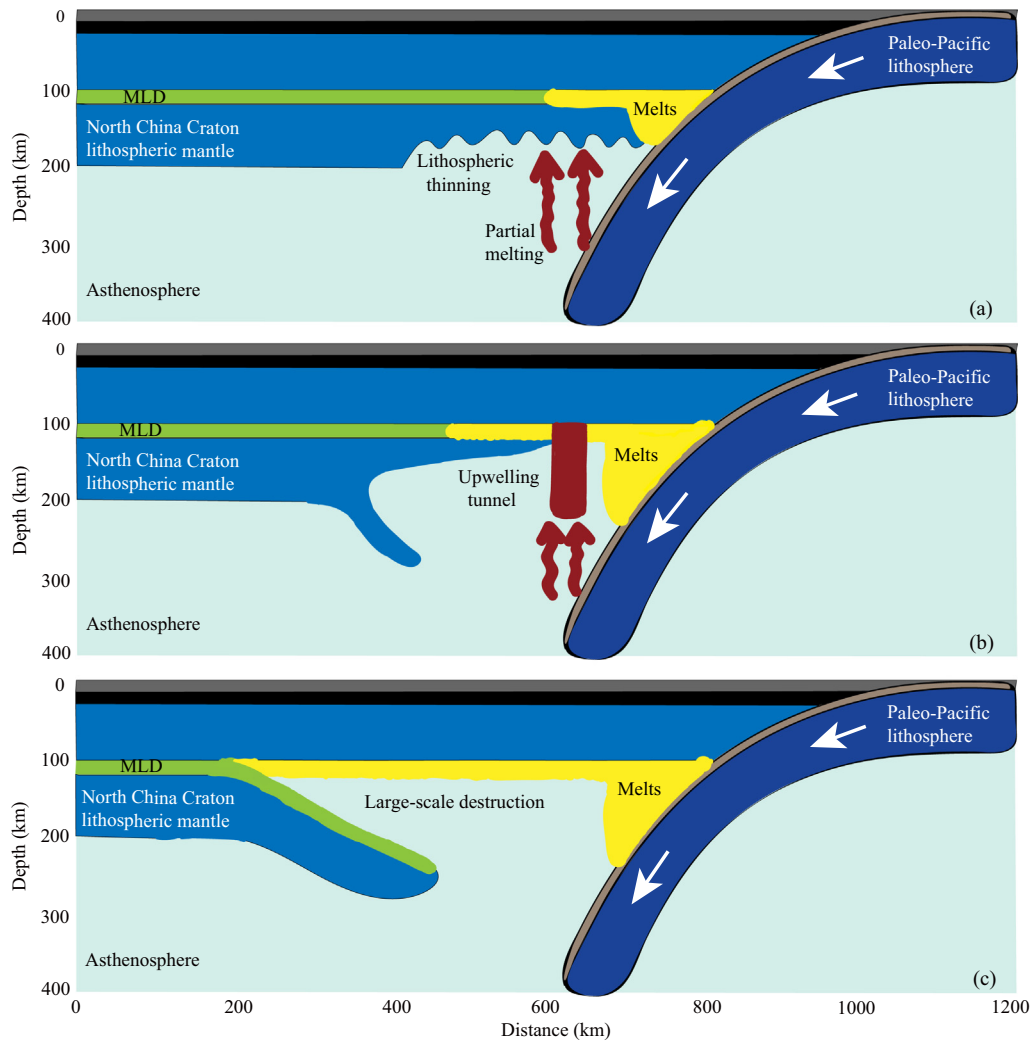


Fig. 14. Schematic interpretation of the geodynamical evolution responsible for the thinning and destruction of the North China Craton controlled by the interaction between the subduction and a weak MLD layer.

predict a ~100 km depth of thinning and a 700 km width of destruction in the cratonic lithospheric mantle, which are consistent with the thinning and destruction extent of the eastern NCC. For the western NCC, the MLD layer was observed in the lithospheric mantle through seismic studies (Chen et al., 2014), however, it still remains to be a stable craton. This could be attributed to the long distance from the Paleo-Pacific subduction zone.

The tectonic interpretation is summarized in Fig. 14. The thinning and destruction of the NCC are resulted by the interaction of the Paleo-Pacific subduction and the presence of a weak MLD layer. The MLD layer contributes to the lithospheric instabilities by decoupling its overlying and underlying lithospheric mantles. On the other hand, subduction-induced partial melting weakens the overriding lithosphere and connects the weak MLD layer with the hot asthenosphere (Fig. 14a and b). Thus the favorable condition for lithosphere delamination results (Bird, 1979). Finally, large-scale delamination of cratonic lithosphere is resulted along the MLD layer (Fig. 14c), which may give a good explanation for the destruction of the eastern part of the North China Craton. It is worth noting that the subduction-induced weakening of overriding lithosphere could take a long time, but the final delamination process is generally fast (Fig. 4c and d), which may explain the peak of magmatism on the eastern NCC occurred in the middle Cretaceous (Tang et al., 2018).

6. Conclusions

We conducted high-resolution thermo-mechanical numerical experiments to systematically investigate the dynamics of the thinning and destruction of the cratonic lithosphere induced by the interaction of subduction and a weak MLD layer. The main conclusions from this comprehensive study include the following:

- (1) The MLD layer plays a significant role in the lithospheric delamination, which however requires coupling with neighboring subduction. The subduction-induced partial melting weakens the lithospheric mantle and thus contributes to the connection between MLD layer and the asthenosphere.
- (2) The thinning and destruction extent of the cratonic lithosphere increases with larger thickness or depth, and lower viscosity of the MLD layer.
- (3) The thinning and destruction of the cratonic lithosphere are favored by thicker oceanic crust (plateau), higher convergence velocity and also larger initial subduction angle.
- (4) The destruction of cratonic lithosphere can occur with the reference density contrast between the lithospheric mantle and asthenosphere larger than -30 kg/m^3 . The larger the density contrast is, the wider destruction extent is expected.

- (5) The interaction between Paleo-Pacific subduction and MLD layer may eventually accelerate the gravitational instability and trigger the thinning and destruction of the eastern North China Craton.

Supplementary data to this article can be found online at <https://doi.org/10.1016/j.gr.2020.01.016>.

Declaration of competing interest

The authors declare that they have no known competing financial interests or personal relationships that could have appeared to influence the work reported in this paper.

Acknowledgements

This work was jointly supported by the National Key Research and Development Program of China (No. 2017YFC1500303), the NSFC projects (41630209, 41688103, 41622404), and the Strategic Priority Research Program (B) of Chinese Academy of Sciences (XDB18000000). Numerical simulations were run with the clusters of National Supercomputer Center in Guangzhou (Tianhe-II). Alan Levander is acknowledged for the helpful discussion.

References

- Abt, D.L., Fischer, K.M., French, S.W., Ford, H.A., Yuan, H.Y., Romanowicz, B., 2010. North American lithospheric discontinuity structure imaged by Ps and Sp receiver functions. *J. Geophys. Res. Solid Earth* 115, B09310. <https://doi.org/10.1029/2009JB006914>.
- Arcay, D., Tric, E., Doin, M.P., 2005. Numerical simulations of subduction zones: effect of slab dehydration on the mantle wedge dynamics. *Phys. Earth Planet. Inter.* 149, 133–153.
- Artemieva, I.M., 2009. The continental lithosphere: reconciling thermal, seismic, and petrologic data. *Lithos* 109, 23–46.
- Aulbach, S., Massuyeau, M., Gaillard, F., 2017. Origins of cratonic mantle discontinuities: a view from petrology, geochemistry and thermodynamic models. *Lithos* 268, 364–382.
- Bird, P., 1979. Continental delamination and the Colorado Plateau. *J. Geophys. Res. Solid Earth* 84, 7561–7571.
- Bittner, D., Schmeling, H., 1995. Numerical modeling of melting processes and induced diapirism in the Lower Crust. *Geophys. J. Int.* 12, 59–70.
- Brace, W.F., Kohlstedt, D.L., 1980. Limits on lithospheric stress imposed by laboratory experiments. *J. Geophys. Res. Solid Earth* 85, 6248–6252.
- Burg, J.P., Gerya, T.V., 2005. The role of viscous heating in Barrovian metamorphism of collisional orogens: thermomechanical models and application to the Lepontine Dome in the Central Alps. *J. Metamorph. Geol.* 23, 75–95.
- Carlson, R.W., Pearson, D.G., James, D.E., 2005. Physical, chemical, and chronological characteristics of continental mantle. *Rev. Geophys.* 43, 353–377.
- Chen, L., 2009. Lithospheric structure variations between the eastern and central North China Craton from S- and P-receiver function migration. *Phys. Earth Planet. Inter.* 173, 216–227.
- Chen, L., 2010. Concordant structural variations from the surface to the base of the upper mantle in the North China Craton and its tectonic implications. *Lithos* 120, 96–115.
- Chen, L., 2017. Layering of subcontinental lithospheric mantle. *Sci. Bull.* 62, 1030–1034.
- Chen, B., Jahn, B.M., Arakawa, Y., Zhai, M.G., 2004. Petrogenesis of the Mesozoic intrusive complexes from the southern Taihang orogeny, north China Craton: elemental and Sr-Nd-Pb isotopic constraints. *Contrib. Mineral. Petrol.* 148, 489–501.
- Chen, L., Wang, T., Zhao, L., Zheng, T.Y., 2008. Distinct lateral variation of lithospheric thickness in the Northeastern North China Craton. *Earth Planet. Sci. Lett.* 267, 56–68.
- Chen, L., Cheng, C., Wei, Z.G., 2009a. Seismic evidence for significant lateral variations in lithospheric thickness beneath the central and western North China Craton. *Earth Planet. Sci. Lett.* 286, 171–183.
- Chen, C.W., Rondenay, S., Evans, R.L., Snyder, B.D., 2009b. Geophysical detection of relict metasomatism from an Archean (approximately 3.5 Ga) subduction zone. *Science* 326, 1089–1091.
- Chen, L., Jiang, M.M., Yang, J.H., Wei, Z.G., Liu, C.Z., Ling, Y., 2014. Presence of an intralithospheric discontinuity in the central and western North China Craton: implications for destruction of the craton. *Geology* 42, 223–226.
- Cheng, H.D., Huang, J.S., 2017. Numerical simulation on the detachment of eclogitic lower crust. *Sci. Sin. Terrae* 47, 82–94.
- Cheng, H.D., Huang, J.S., Fu, R.S., 2016. Numerical simulation on convective thinning of the cratonic lithosphere. *Chin. J. Geophys.* 59, 1293–1308.
- Clauser, C., Huenges, E., 1995. Thermal conductivity of rocks and minerals. AGU reference shelf 3, 105–126.
- Dawson, J.B., Smith, J.V., 1977. The MARID (mica-amphibole-rutile-ilmenite-diopside) suite of xenoliths in kimberlite. *Geochim. Cosmochim. Acta* 41, 309–310.
- Dawson, J.B., Smith, J.V., 1988. Metasomatized and veined upper-mantle xenoliths from Pello Hill, Tanzania: evidence for anomalously-light mantle beneath the Tanzanian sector of the East African Rift Valley. *Contrib. Mineral. Petrol.* 100, 510–527.
- Dessai, A.G., Markwick, A., Vaselli, O., Downes, H., 2004. Granulite and pyroxenite xenoliths from the Deccan Trap: insight into the nature and composition of the lower lithosphere beneath Cratonic India. *Lithos* 78, 263–290.
- Djomani, Y., O'Reilly, S., Griffin, W.L., Morgan, P., 2001. The density structure of subcontinental lithosphere through time. *Earth Planet. Sci. Lett.* 184, 605–621.
- Downes, H., MacDonald, R., Upton, B.G.J., Cox, K.G., Bodinier, J.L., Mason, P.R.D., James, D., Hill, P.G., Carter Hearn, B., 2004. Ultramafic xenoliths from the Bearpaw Mountains, Montana, USA: evidence for multiple metasomatic events in the lithospheric mantle beneath the Wyoming craton. *J. Petrol.* 45, 1631–1662.
- Fischer, K.M., Ford, H.A., Abt, D.L., Rychert, C.A., 2010. The lithosphere–asthenosphere boundary. *Annu. Rev. Earth Planet. Sci.* 38, 55–575.
- Gao, S., Rudnick, R.L., Carlson, R.W., McDonough, W.F., Liu, Y.S., 2002. Re-Os evidence for replacement of ancient mantle lithosphere beneath the North China craton. *Earth Planet. Sci. Lett.* 198, 307–322.
- Gerya, T.V., Meilich, F.I., 2011. Geodynamic regimes of subduction under an active margin: effects of rheological weakening by fluids and melts. *J. Metamorph. Geol.* 29, 7–31.
- Gerya, T.V., Yuen, D.A., 2003a. Characteristics-based marker-in-cell method with conservative finite-differences schemes for modeling geological flows with strongly variable transport properties. *Phys. Earth Planet. Inter.* 140, 293–318.
- Gerya, T.V., Yuen, D.A., 2003b. Rayleigh–Taylor instabilities from hydration and melting propel 'cold plumes' at subduction zones. *Earth Planet. Sci. Lett.* 212, 47–62.
- Griffin, W.L., Andi, Z., O'Reilly, S.Y., Ryan, C.G., 1998. Phanerozoic evolution of the lithosphere beneath the Sino-Korean Craton. *Manag. Dyn.* 27, 107–126.
- Griffin, W.L., Doyle, B.J., Ryan, C.G., Pearson, N.J., Suzanne, Y.O., Davies, R., Kivi, K., Van Acherbergh, E., Natapov, L.M., 1999a. Layered mantle lithosphere in the Lac de Gras area, Slave craton: Composition, structure and origin. *J. Petrol.* 40, 705–727.
- Griffin, W.L., Ryan, C.G., Kaminsky, F.V., O'Reilly, S.Y., Natapov, L.M., Win, T.T., Kinny, P.D., Ilupin, I.P., 1999b. The Siberian lithosphere traverse: Mantle terranes and the assembly of the Siberian Craton. *Tectonophysics* 310, 1–35.
- Griffin, W.L., O'Reilly, S.Y., Doyle, B.J., Pearson, N.J., Coopersmith, H., Kivi, K., Malkovets, V., Pokhilenko, N., 2004. Lithosphere mapping beneath the north American plate. *Lithos* 77, 873–922.
- Hansen, L.N., Zimmerman, M.E., Kohlstedt, D.L., 2012. Laboratory measurements of the viscous anisotropy of olivine aggregates. *Nature* 492, 415–418.
- He, L.J., 2014. Numerical modeling of convective erosion and peridotite–melt interaction in big mantle wedge: implications for the destruction of the North China Craton. *J. Geophys. Res. Solid Earth* 119, 3662–3677.
- Hofmeister, A.M., 1999. Mantle values of thermal conductivity and the geotherm from phonon lifetimes. *Science* 283, 1699–1706.
- Hopper, E., Ford, H.A., Fischer, K.M., Lekic, V., Fouch, M.J., 2014. The lithosphere–asthenosphere boundary and the tectonic and magmatic history of the northwestern United States. *Earth Planet. Sci. Lett.* 402, 69–81.
- Howarth, G.H., Barry, P.H., Pernet-Fisher, J.F., Baziotis, I.P., Pokhilenko, N.P., Pokhilenko, L.N., Bodnar, R.J., Taylor, L.A., Agashev, A.M., 2014. Superplume metasomatism: evidence from Siberian mantle xenoliths. *Lithos* 184, 209–224.
- Huangfu, P.P., Wang, Y.J., Cawood, P.A., Li, Z.H., Fan, W.M., Gerya, T.V., 2016. Thermomechanical controls of flat subduction: insights from numerical modeling. *Gondwana Res.* 40, 170–183.
- Ji, S.C., Zhao, P.L., 1993. Flow laws of multiphase rocks calculated from experimental data on the constituent phases. *Earth Planet. Sci. Lett.* 117, 181–187.
- Jordan, T.H., 1988. Structure and formation of the continental tectosphere. *J. Petrol.* 1, 11–37.
- Jull, M., Kelemen, P.B., 2001. On the conditions for lower crustal convective instability. *J. Geophys. Res.* 106, 6423–6446.
- Karato, S.I., Jung, H., 2003. Effects of pressure on high-temperature dislocation creep in olivine. *Philos. Mag.* 83, 401–414.
- Karato, S., Ogluboji, T., Park, J., 2015. Mechanisms and geologic significance of the mid-lithosphere discontinuity in the continents. *Nat. Geosci.* 8, 509–514.
- Karmalkar, N.R., Duraiswami, R.A., Chalapathi, Rao, N.V., Paul, D.K., 2009. Mantle-derived mafic-ultramafic xenoliths and the nature of Indian subcontinental lithosphere. *J. Geol. Soc. India* 73, 657–679.
- Kennett, B.L.N., Sippl, C., 2018. Lithospheric discontinuities in Central Australia. *Tectonophysics* 744, 10–22.
- Kirby, S.H., 1983. Rheology of the Lithosphere. *Rev. Geophys.* 21, 1458–1487.
- Kirby, S.H., Kronenberg, A.K., 1987. Rheology of the lithosphere: selected topics. *Rev. Geophys.* 25, 1219–1244.
- Kumar, A., Heaman, L.M., Manikyamba, C., 2007. Mesoproterozoic kimberlites in south India: a possible link to ~1.1 Ga global magmatism. *Precambrian Res.* 154, 192–204.
- Lee, C.T.A., Cheng, X., Horodyskyj, U., 2006. The development and refinement of continental arcs by primary basaltic magmatism, garnet pyroxenite accumulation, basaltic recharge and delamination: insights from the Sierra Nevada, California. *Contrib. Mineral. Petrol.* 151, 222–242.
- Lee, C.T.A., Luffi, P., Chin, E.J., 2011. Building and destroying continental mantle. *Annu. Rev. Earth Planet. Sci.* 39, 59–90.
- Lei, T., Li, Z.H., Liu, M., 2019. Removing mantle lithosphere under orogens: delamination versus convective thinning. *Geophys. J. Int.* 219, 877–896.
- Li, Z.H., Gerya, T.V., Burg, J.P., 2010. Influence of tectonic overpressure on P-T paths of HP-UHP rocks in continental collision zones: Thermomechanical modeling. *J. Metamorph. Geol.* 28, 227–247.
- Li, Z.H., Xu, Z., Gerya, T.V., 2011. Flat versus steep subduction: contrasting modes for the formation and exhumation of high- to ultrahigh-pressure rocks in continental collision zones. *Earth Planet. Sci. Lett.* 301, 65–77.
- Li, Z.H., Liu, M.Q., Gerya, T.V., 2015. Material transportation and fluid–melt activity in the subduction channel: Numerical modeling. *Sci. China Earth Sci.* 58, 1251–1268.
- Li, Z.H., Liu, M., Gerya, T.V., 2016. Lithosphere delamination in continental collisional orogens: a systematic numerical study. *J. Geophys. Res. Solid Earth* 121, 5186–5211.

- Li, Z.H., Gerya, T.V., Connolly, J., 2019. Variability of subducting slab morphologies in the mantle transition zone: Insight from petrological-thermomechanical modeling. *Earth Sci. Rev.* 196, 102874.
- Liao, J., Gerya, T.V., 2014. Influence of lithospheric mantle stratification on craton extension: Insight from two-dimensional thermo-mechanical modeling. *Tectonophysics* 631, 50–64.
- Liao, J., Gerya, T.V., Wang, Q., 2013. Layered structure of the lithospheric mantle changes dynamics of craton extension. *Geophys. Res. Lett.* 40, 5861–5866.
- Liu, M., Li, Z.H., 2018. Dynamics of thinning and destruction of the continental cratonic lithosphere: numerical modeling. *Sci. China Earth Sci.* 61, 823–852.
- Liu, M.Q., Li, Z.H., Yang, S.H., 2017. Diapir versus along-channel ascent of crustal material during plate convergence: constrained by the thermal structure of subduction zones. *J. Asian Earth Sci.* 145, 16–36.
- Liu, L., Morgan, J.P., Xu, Y., Menzies, M., 2018a. Craton destruction part I: cratonic keel delamination along a weak mid-lithospheric discontinuity layer. *J. Geophys. Res. Solid Earth* 123, 10040–10068.
- Liu, L., Morgan, J.P., Xu, Y., Menzies, M., 2018b. Craton destruction part II: evolution of cratonic lithosphere after a rapid keel delamination event. *J. Geophys. Res. Solid Earth* 123, 10069–10090.
- Lu, F.X., Han, Z.G., Zheng, J.P., Ren, Y.X., 1991. Characteristics of Paleozoic mantle-lithosphere in Fuxian, Liaoning province (in Chinese). *Geol. Sci. Technol. Inform.* 10, 2–19.
- Menzies, M., Xu, Y.G., 1998. *Geodynamics of the North China Craton*. American Geophysical Union, Washington, DC, pp. 155–165.
- Menzies, M., Xu, Y.G., Zhang, H.F., Fan, W.M., 2007. Integration of geology, geophysics and geochemistry: a key to understanding the North China Craton. *Lithos* 96, 1–21.
- Nita, B., Maurya, S., Montagner, J.P., 2016. Anisotropic tomography of the European lithospheric structure from surface wave studies. *Geochem. Geophys. Geosyst.* 17, 2015–2033.
- O'Reilly, S.Y., Griffin, W.L., 2010. The continental lithosphere-asthenosphere boundary: can we sample it? *Lithos* 120, 1–13.
- Qiao, Y.C., Guo, Z.Q., Shi, Y.L., 2012. Numerical simulation of a possible thinning mechanism of the North China Craton-Gravitational instability delamination induced by lower crust eclogite (in Chinese). *Chin. J. Geophys.* 55, 4249–4256.
- Qiao, Y.C., Guo, Z.Q., Shi, Y.L., 2013. Thermal convection thinning of the North China Craton: numerical simulation (in Chinese). *Sci. China Earth Sci.* 43, 642–652.
- Rader, E., Emry, E., Schmerr, N., Frost, D., Cheng, C., Menard, J., Yu, C., Geist, D., 2015. Characterization and petrological constraints of the midlithospheric discontinuity. *Geochem. Geophys. Geosyst.* 16, 3484–3504.
- Ranalli, G., 1995. *Rheology of the Earth, Deformation and Flow Process in Geophysics and Geodynamics*. 2nd ed. Chapman and Hall, London.
- Ranalli, G., Murphy, D.C., 1987. Rheological stratification of the lithosphere. *Tectonophysics* 132, 281–295.
- Rao, K., Dhakate, M., Nayak, S., 2001. Petrology and mineralogy of mantle xenoliths of Wajrakarur and Narayanpet kimberlite fields, Andhra Pradesh, India. *Geol. Surv. India Spec. Publ.* 58, 577–591.
- Rao, N.V.C., Wu, F.Y., Mitchell, R.H., Li, Q.L., Lehmann, B., 2013. Mesoproterozoic U-Pb ages, trace element and Sr-Nd isotopic composition of perovskite from kimberlites of the Eastern Dharwar craton, southern India: distinct mantle sources and a widespread 1.1 Ga tectonomagmatic event. *Chem. Geol.* 353, 48–64.
- Read, G., Grutter, H., Winter, S., Luckman, N., Gaunt, F., Thomsen, F., 2004. Stratigraphic relations, kimberlite emplacement and lithospheric thermal evolution, Quirico Basin, Minas Gerais State, Brazil. *Lithos* 77, 803–818.
- Schmeling, H., Babeyko, A.Y., Enns, A., Faccenna, C., Funicello, F., Gerya, T.V., Golabek, G.J., Grigull, S., Kaus, B.J.P., Morra, G., Schmalholz, S.M., van Hunen, J., 2008. A benchmark comparison of spontaneous subduction models—towards a free surface. *Phys. Earth Planet. Inter.* 171, 198–223.
- Schmidt, M.W., Poli, S., 1998. Experimentally based water budgets for dehydrating slabs and consequences for arc magma generation. *Earth Planet. Sci. Lett.* 163, 361–379.
- Schubert, G., Turcotte, D.L., Olson, P., 2001. *Mantle Convection in the Earth and Planets*. Cambridge University Press, Cambridge.
- Schutt, D.L., Leshner, C.E., 2006. Effects of melt depletion on the density and seismic velocity of garnet and spinel lherzolite. *J. Geophys. Res.* 111, B05401.
- Selway, K., Ford, H., Kelemen, P., 2015. The seismic mid-lithosphere discontinuity. *Earth Planet. Sci. Lett.* 414, 45–57.
- Shi, Y.N., Wei, D.P., Huangfu, P.P., Li, Z.H., Liu, M.X., 2019. Dynamics of thinning of overriding continental lithosphere induced by oceanic plate subduction: numerical modeling. *Chin. J. Geophys.* 62, 63–77.
- Sleep, N.H., 2003. Survival of Archean cratonic lithosphere. *J. Geophys. Res.* 108, 2302.
- Sobolev, S., Sobolev, A., Kuzmin, D., Krivolutskaia, N., Petrunin, A., Arndt, N., Radko, V., Vasiliev, Y., 2011. Linking mantle plumes, large igneous provinces and environmental catastrophes. *Nature* 477, 312–316.
- Sodoudi, F., Yuan, X., Kind, R., Lebedev, S., Adam, J.M.C., Kästle, E., Tilmann, F., 2013. Seismic evidence for stratification in composition and anisotropic fabric within the thick lithosphere of Kalahari Craton. *Geochem. Geophys. Geosyst.* 14, 5393–5412.
- Stüwe, K., 1995. Thermal buffering effects at the solidus. Implications for the equilibration of partially melted metamorphic rocks. *Tectonophysics* 248, 39–51.
- Sun, W., Fu, L., Erdinc, S., Zhao, L., 2018. Insights into layering in the cratonic lithosphere beneath western Australia. *J. Geophys. Res. Solid Earth* 123, 1405–1418.
- Tang, Y.J., Zhang, H.F., Ying, J.F., Su, B.X., 2013. Widespread refertilization of cratonic and circum-cratonic lithospheric mantle. *Earth-Sci. Rev.* 118, 45–68.
- Tang, J., Xu, W.L., Wang, F., Ge, W.C., 2018. Subduction history of the Paleo-Pacific slab beneath Eurasian continent: Mesozoic-Paleogene magmatic records in Northeast Asia. *Sci. China Earth Sci.* 61, 527–559.
- Thybo, H., Perchuc, E., 1997. The seismic 8° discontinuity and partial melting in continental mantle. *Science* 275, 1626–1629.
- Tommasi, A., Knoll, M., Vauchez, A., Signorelli, J.W., Thoraval, C., Logé, R., 2009. Structural reactivation in plate tectonics controlled by olivine crystal anisotropy. *Nat. Geosci.* 2, 423–427.
- Turcotte, D.L., Schubert, G., 2002. *Geodynamics*. Cambridge University Press, Cambridge.
- Wang, Z., Kusky, T.M., 2019. The importance of a weak mid-lithospheric layer on the evolution of the cratonic lithosphere. *Earth-Sci. Rev.* 190, 557–569.
- Wang, Z., Kusky, T.M., Capitanio, F.A., 2016. Lithosphere thinning induced by slab penetration into a hydrous mantle transition zone. *Geophys. Res. Lett.* 43, 11567–11577.
- Wang, Z., Kusky, T.M., Capitanio, F.A., 2018. On the role of lower crust and mid-lithosphere discontinuity for cratonic lithosphere delamination and recycling. *Geophys. Res. Lett.* 45, 7425–7433.
- White, R.S., McKenzie, D., O'Nions, R.K., 1992. Oceanic crustal thickness from seismic measurements and rare earth element inversions. *J. Geophys. Res. Solid Earth* 97, 19683–19715.
- Windley, B.F., Maruyama, S., Xiao, W.J., 2010. Delamination/thinning of sub-continental lithospheric mantle under Eastern China: the role of water and multiple subduction. *Am. J. Sci.* 310, 1250–1293.
- Wölbner, I., Rümpler, G., Link, K., Sodoudi, F., 2012. Melt infiltration of the lower lithosphere beneath the Tanzania craton and the Albertine rift inferred from S receiver functions. *Geochem. Geophys. Geosyst.* 13, 1–20.
- Wu, F.Y., Xu, Y.G., Gao, S., Zheng, J.P., 2008. Lithospheric thinning and destruction of the North China Craton (in Chinese). *Acta Petrol. Sin.* 24, 1145–1174.
- Wu, F.Y., Xu, Y.G., Zhu, R.X., Zhang, G.W., 2014. Thinning and destruction of the cratonic lithosphere: a global perspective. *Sci. China Earth Sci.* 57, 2878–2890.
- Wu, F.Y., Yang, J.H., Xu, Y.G., Wilde, S.A., Walker, R.J., 2019. Destruction of the North China Craton in the Mesozoic. *Annu. Rev. Earth Planet. Sci.* 47, 173–195.
- Xu, Y.G., 2001. Thermo-tectonic destruction of the Archean lithospheric keel beneath the Sino-Korean Craton in China: evidence, timing and mechanism. *Phys. Chem. Earth Solid Earth Geod.* 26, 747–757.
- Xu, Y.G., Blusztajn, J., Ma, J.L., Suzuki, K., Liu, J.F., Hart, S.R., 2008. Late Archean to Early Proterozoic lithospheric mantle beneath the western North China Craton: Sr-Nd-Os isotopes of peridotite xenoliths from Yangyuan and Fansi. *Lithos* 102, 25–42.
- Xu, Y.G., Li, H.Y., Pang, C.J., He, B., 2009. On the timing and duration of the destruction of the North China Craton. *Chin. Sci. Bull.* 54, 3379.
- Yang, J.H., Wu, F.Y., Wilde, S.A., 2003. A review of the geodynamic setting of large-scale Late Mesozoic gold mineralization in the North China Craton: an association with lithospheric thinning. *Ore Geol. Rev.* 23, 125–152.
- Yang, J.H., Sun, J.F., Zhang, M., Wu, F.Y., Wilde, S.A., 2012. Petrogenesis of silica-saturated and silica-undersaturated syenites in the northern North China Craton related to post-collisional and intraplate extension. *Chem. Geol.* 328, 149–167.
- Yuan, H., Romanowicz, B., 2010. Lithospheric layering in the north American craton. *Nature* 466, 1063–1068.
- Zhai, M.G., 2008. Lower crust and lithospheric mantle beneath the North China Craton before the Mesozoic lithosphere disruption. *Acta Petrol. Sin.* 24, 2185–2204.
- Zhai, M.G., Meng, Q.R., Liu, J.M., Hou, Q.L., Hu, S.B., Li, Z., Zhang, H.F., Liu, W., Shao, J.A., Zhu, R.X., 2004. Geological features of Mesozoic tectonic regime inversion in Eastern North China and implication for geodynamics (in Chinese). *Earth Sci. Front.* 3, 285–297.
- Zhang, H.F., Sun, M., Zhou, X.H., Fan, W.M., Zhai, M.G., Yin, J.F., 2002. Mesozoic lithosphere destruction beneath the North China Craton: evidence from major, trace element, and Sr-Nd-Pb isotope studies of Fangcheng basalts. *Contrib. Mineral. Petrol.* 144, 241–253.
- Zhang, H.F., Sun, M., Zhou, X.H., Zhou, M.F., Fan, W.M., Zheng, J.P., 2003. Secular evolution of the lithosphere beneath the eastern North China Craton: evidence from Mesozoic basalts and high-Mg andesites. *Geochim. Cosmochim. Acta* 67, 4373–4387.
- Zheng, T.Y., Duan, Y.H., Xu, W.W., Ai, Y.S., 2017. A seismic model for crustal structure in North China Craton. *Earth Planet. Phys.* 1, 26–34.
- Zhu, R.X., Zheng, T.Y., 2009. Destruction geodynamics of the North China Craton and its Paleoproterozoic plate tectonics. *Chin. Sci. Bull.* 54, 3354.
- Zhu, R.X., Xu, Y.G., Zhu, G., Zhang, H.F., Xia, Q.K., Zheng, T.Y., 2012. Destruction of the North China Craton. *Sci. China Earth Sci.* 55, 1565–1587.